JGR Oceans

RESEARCH ARTICLE

10.1029/2023JC020077

Intrinsic Versus Wind-Forced Great Whirl Non-Seasonal Variability

Kwatra Sadhvi[1], Iyyappan Suresh[2,3], Matthieu Lengaigne[4], Takeshi Izumo[5], Thierry Penduff[6], Jean-Marc Molines[6], Aftab A. Can[1], and Jérôme Vialard[7]

[1]Goa University, Taleigao, India, [2]CSIR-National Institute of Oceanography (CSIR-NIO), Panaji, India, [3]Digital University Kerala (DUK), Trivandrum, India, [4]MARBEC, University of Montpellier, CNRS, IFREMER, IRD, Sete, France, [5]UMR 241 EIO, Université de Polynésie Française, Tahiti, France, [6]Université Grenoble Alpes, CNRS, INRAE, IRD, Grenoble INP, Institut des Géosciences de l'Environnement (IGE), Grenoble, France, [7]LOCEAN/IPSL, IRD-Sorbonne Universités-CNRS-MNHN, Paris, France

Key Points:

- The Great Whirl (GW) non-seasonal variability is dominated by ∼100-km northward or southward shifts relative to its climatological position
- Those shifts induce sea level, surface temperature and chlorophyll signals
- Those GW displacements have a fast (∼20 days) intrinsic variability component and a slower, seasonal forced component

Correspondence to:

J. Vialard,
jerome.vialard@ird.fr

Citation:

Sadhvi, K., Suresh, I., Lengaigne, M., Izumo, T., Penduff, T., Molines, J.-M., et al. (2024). Intrinsic versus wind-forced Great Whirl non-seasonal variability. *Journal of Geophysical Research: Oceans*, *129*, e2023JC020077. https://doi.org/10.1029/2023JC020077

Received 6 JUN 2023
Accepted 18 JAN 2024

Author Contributions:

Conceptualization: Iyyappan Suresh, Matthieu Lengaigne, Takeshi Izumo, Jérôme Vialard
Data curation: Jean-Marc Molines
Formal analysis: Kwatra Sadhvi
Funding acquisition: Iyyappan Suresh, Matthieu Lengaigne, Jérôme Vialard
Investigation: Kwatra Sadhvi, Iyyappan Suresh
Methodology: Kwatra Sadhvi, Iyyappan Suresh, Matthieu Lengaigne, Takeshi Izumo, Jérôme Vialard
Resources: Iyyappan Suresh, Thierry Penduff, Jean-Marc Molines, Aftab A. Can
Software: Kwatra Sadhvi, Iyyappan Suresh
Supervision: Iyyappan Suresh, Matthieu Lengaigne, Takeshi Izumo, Jérôme Vialard
Validation: Kwatra Sadhvi
Visualization: Kwatra Sadhvi

Abstract The Great Whirl (GW) is a quasi-permanent anticyclonic eddy that appears every summer monsoon offshore of the Somalia upwelling. The annual cycle of the GW is well described, but deviations from its mean seasonal cycle (hereafter non-seasonal variability) have been less explored. Satellite observations reveal that the leading mode of summer non-seasonal sea-level variability in this region is associated with ∼100-km northward or southward GW shifts from its climatological position. Northward shifts are associated with a stronger GW, and two cold, productive coastal upwelling wedges at 5°N and 10°N. Southward shifts are associated with a weaker GW, no wedge at 5°N and a single stronger-than-usual cold and productive wedge at 10°N. An eddy-permitting (25-km resolution) 50-member ensemble ocean simulation reproduces this GW variability well. It indicates that the non-seasonal GW variability has a short ∼20 days timescale intrinsic component, associated with the GW interaction with mesoscale eddies, and a lower-frequency, ∼100 days externally forced component. Intrinsic variability dominates at both subseasonal (two thirds of the variance) and interannual timescales (57% of the variance). The externally forced signal results from shifts in the probability distribution of the subseasonal GW position (e.g., more likely northward than southward shifted instantaneous GW positions over a season). The mechanism for this external forcing is not entirely clear, but it appears to be related to the Rossby wave response to offshore wind stress curl forcing, which evolves into a north-south dipole that projects onto the GW variability pattern.

Plain Language Summary The Great Whirl (GW) is a ∼500-km diameter oceanic eddy that forms each summer off the Somalia coast. The GW influences the temperature and biological productivity of the Somalia coastal upwelling. The GW seasonal cycle, including its northward movement at the end of the monsoon, is known. Here, we study deviations from this mean seasonal cycle. The GW exhibits fast (typically 20 days long), ∼100-km northward or southward displacements. These displacements result from interactions with smaller neighboring oceanic eddies, and are hence the consequence of an intrinsic ocean dynamics, rather than atmospheric forcing. The GW is more pronounced when displaced northward, and the Somalia coastal upwelling has two clear "wedges" of cold, plankton-rich water at 5° and 10°N. When displaced southward, the GW is less pronounced, and there is a single, stronger-than-usual wedge of cold water at 10°N. We also show that atmospheric forcing can induce seasonal GW displacements, by making, for example, northward events more likely than the southward. Thus, the seasonal mean GW position has both a predictable (due to atmospheric forcing) and slightly larger unpredictable (due to interactions with eddies) component. We propose that the atmospheric forcing influences the fast oscillations of the GW through slow oceanic adjustment to wind variations further east.

1. Introduction

Some oceanic features are so obvious to navigators that they were described long before modern oceanographers began studying them. One of them is the "great whirl of current" reported in the sailing directory of the Indian Ocean (Findlay, 1866). This feature was observed during the southwest monsoon in the western Arabian Sea, about 150 nautical miles (∼277.8 km) south of Socotra Island. It is 400–500 km in diameter and has surface currents up to 2.5 m s^{-1}. In August-September 1964, oceanographic cruises participating in the first International Indian Ocean Expedition (IIOE) provided a similar description of the surface circulation in this region (Swallow

Writing – original draft: Jérôme Vialard
Writing – review & editing: Kwatra Sadhvi, Iyyappan Suresh, Matthieu Lengaigne, Takeshi Izumo, Thierry Penduff

& Bruce, 1966), suggesting that a quasi-stationary eddy appears at this location during each summer monsoon. Subsequent observational studies have indeed confirmed that an anticyclonic eddy forms off Somalia prior to the monsoon onset, and remains present throughout the southwest monsoon (e.g., Bruce, 1979; Swallow & Fieux, 1982). This eddy is now known as the "Great Whirl" (hereafter GW).

The GW is not only important for navigation: with an offshore transport of about 58 Sv (Fischer et al., 1996), it exports cold, productive and nutrient-rich water from the Somalia upwelling to the open ocean (Figures 1b and 1c; Hood et al., 2017; Vinayachandran et al., 2021), as evidenced by the cold filaments extending far offshore (e.g., Hitchcock et al., 2000). On the other hand, the return flow of the southern branch of the GW suppresses the upwelling around 6°N (Figures 1a and 1b), effectively splitting the Somalia upwelling into two "cold wedges" (e.g., Schott & McCreary, 2001). The GW thus plays an important role in shaping the coastal upwelling and its offshore exports, and is thus relevant for both regional climate and high marine productivity during summer monsoon. Indeed, the intensity of the Somalia upwelling is thought to modulate the atmospheric water vapor uptake and monsoon rainfall over the Indian subcontinent (Izumo et al., 2008), and GW and other mesoscale features have a clear atmospheric signature in this region (Seo, 2017; Vecchi et al., 2004). Satellite observations further indicate a clear chlorophyll minimum within the GW, but higher values in filaments along its periphery (Figure 5 of Dai et al., 2021). Modeling studies (Kawamiya, 2001; Resplandy et al., 2011; Young & Kindle, 1994) confirm that lateral advection around the GW is a strong contributor to the nutrients supply to the central Arabian Sea. Finally, the GW is also a pre-eminent feature in the spatial distribution of non-tuna species pelagic fishes in the western Indian Ocean (Orúe et al., 2020), suggesting that this oceanic feature also structures the ecosystem at higher trophic levels. For all of these reasons, it is therefore important to properly describe and understand the GW dynamics and variability.

Decades of oceanographic cruises and the advent of satellite oceanography now allow for a detailed description of the GW lifecycle. The GW is characterized by a sea level high (Figure 1a) and can thus be tracked from satellite data (e.g., Beal & Donohue, 2013; Cao & Hu, 2015; Melzer et al., 2019; Trott et al., 2017; Wang et al., 2019). A closed whirl of currents (Figure 1b) first appears off Somalia on average in April (Figure 2a; Beal & Donohue, 2013), synchronized with the arrival of a Rossby wave radiated from the west coast of India (Shankar & Shetye, 1997). This whirl intensifies in June, coinciding with the onset of the southwest monsoon winds, remains strong through July–September (Figure 2) and dissipates after the end of the summer monsoon in October (Beal & Donohue, 2013) or later (Melzer et al., 2019).

Many mechanisms have been proposed to date to explain the GW. Early studies suggested that the GW is a linear response to the strong anticyclonic curl east of the Findlater jet, resulting from energy accumulation associated with the coastal reflection of long downwelling Rossby waves into short Rossby waves (e.g., Schott & Quadfasel, 1982). However, several studies pointed out that linear dynamics is not sufficient to describe the GW, due to the 30%–70% deviations from geostrophy in the region (e.g., Beal & Donohue, 2013; Fischer et al., 1996; Knox & Anderson, 1985), and the fact that the strong offshore curl is not a necessary condition for the GW generation (McCreary & Kundu, 1988). Jensen (1993) showed that barotropic instability plays an important role during the GW strengthening phase. Some modeling works emphasized the importance of a slanted (rather than meridional) coastline to block the GW northward propagation (Cox, 1979; McCreary & Kundu, 1988) while other studies suggested that this effect is weak (Anderson, 1981; Vic et al., 2014). The recent modeling study by Vic et al. (2014) confirms the seeding role of the basin-scale annual Rossby wave in the GW generation, as mentioned by Beal and Donohue (2013), and the joint role of the anticyclonic curl and barotropic instability in the GW strengthening. But overall, there is no firmly established, consensus theory on the mechanisms that contribute to the GW lifecycle.

Because of its aforementioned impact on marine productivity and climate, several studies have examined the GW deviations from this mean seasonal cycle (hereafter non-seasonal variability), including both intraseasonal and interannual variations. Beal and Donohue (2013) noted strong intraseasonal variations in the GW position, and attributed this feature to mutual advection by flanking eddies. Numerous studies have found significant interannual variations in most of the GW characteristics, including onset and decay dates (e.g., Melzer et al., 2019; Wang et al., 2019), size (Trott et al., 2018) and position (e.g., Beal & Donohue, 2013; Cao & Hu, 2015; Melzer et al., 2019; Trott et al., 2018; Wang et al., 2019). None of these studies found a clear link between the GW position and large-scale climate modes such as the El Niño Southern Oscillation (ENSO), the Indian Ocean Dipole (IOD), or the intensity of the monsoon. Melzer et al. (2019) and Wang et al. (2019) reported that the GW position appeared to have a bimodal distribution during its peak season, and a more scattered location during its

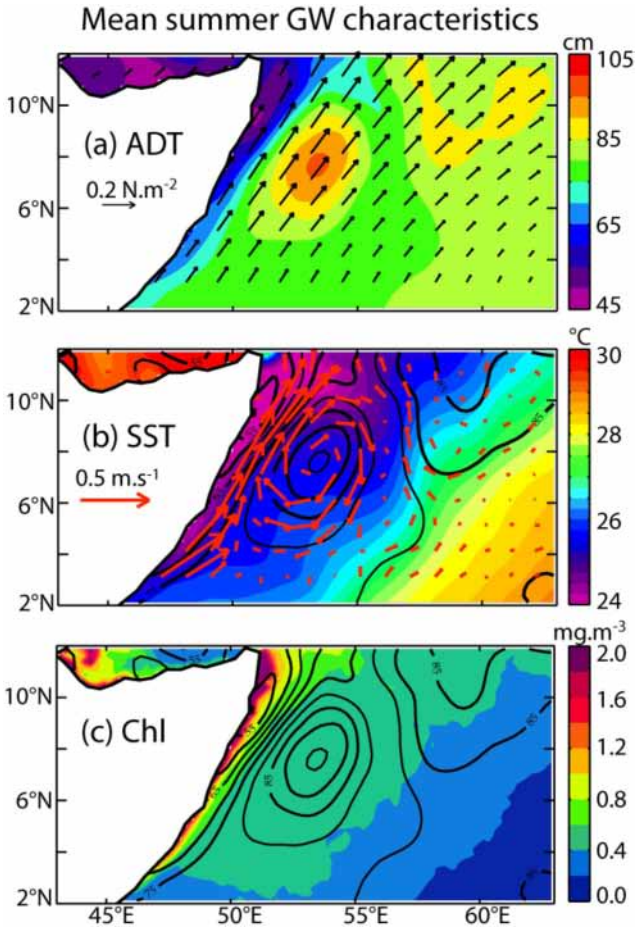

Figure 1. Observed July, August, and September (JAS) climatology of (a) Absolute Dynamic Topography (ADT; shading; cm) and wind-stress (vectors, $N.m^{-2}$); (b) Sea Surface Temperature (SST; shading; °C) and surface currents (red vectors, $m.s^{-1}$)); and (c) surface chlorophyll (SChl; shading; $mg.m^{-3}$) for the 2003–2015 period. The JAS climatological ADT contours (cm; 5-cm intervals) is overlaid on panels (b, c).

decay. Santos et al. (2015) found a dipolar trend in sea surface temperature and height over the last decades, attributed to a ∼1.5° southward migration of the GW.

Early studies reported a small GW interannual variability when forcing an eddy-permitting non-linear reduced gravity model with climatological winds (Luther & O'Brien, 1985), suggesting that the GW interannual variability is largely wind-driven. In contrast, subsequent studies with eddy-permitting primitive equation models have shown that there is a lot of internal variability in the GW region (Jochum & Murtugudde, 2005; Sengupta et al., 2001; Wirth et al., 2002). In particular, Wirth et al. (2002) showed that the central latitude of the GW exhibits a clear interannual variability even when forced by a repeating climatological cycle, and that this variability is strongly enhanced as lateral friction is decreased.

Overall, observations indicate a clear interannual variability of the GW, which cannot be clearly attributed to wind forcing or large-scale climate signals. Modeling studies suggest that at least some of the interannual GW variability is internally driven. The present study aims to better describe the non-seasonal GW variability. We will not only document this variability in terms of sea level, but also its imprint on Sea Surface Temperature (hereafter, SST) and Surface Chlorophyll (hereafter, SChl), which are two markers of the offshore export of coastal upwelled water. We will also estimate the relative contributions of intrinsic and forced (potentially associated with large-scale climate modes) variability to the GW, and discuss potential mechanisms of the forced response. To this end, we will use satellite data to describe observed sea level, SST and SChl signals. We also use the 50-member eddy-permitting (1/4° resolution) global ensemble simulations performed during the OCCIPUT project (Penduff et al., 2014), based on the NEMO ocean general circulation model. All the members in the OCCIPUT ensemble use the same realistic atmospheric forcing over 1961–2016, and only differ through small perturbations in their January 1961 initial conditions. This results in different realizations of the intrinsic oceanic variability in each member of the ensemble, while these members share a common response to the external atmospheric forcing (e.g., Bessières et al., 2017). This allows to separately estimate the internally generated and forced components of the oceanic variability (e.g., Sérazin et al., 2017).

The paper is organized as follows. Section 2 describes the satellite data sets, simulations (OCCIPUT; NEMO-based simulations and those from a linear model) and methods used in this paper. Section 3 presents our observational analyses and highlights coherent sea level, SST and SChl signals associated with non-seasonal variability in the central latitude of the GW. In Section 4, we show that intrinsic variability dominates the GW non-seasonal variability at intraseasonal timescales in OCCIPUT, but that the internally generated and atmospherically forced GW fluctuations have the same patterns for the seasonal (July–September) average. We further discuss the potential mechanisms and climate drivers of the wind-forced signals. Section 5 proposes a brief summary and a discussion of our results against those of previous studies.

2. Data, Model, and Methods

2.1. Data and Model

The spatial resolution, period that we use, references and version of each data set we use is listed in Table 1. We use the DUACS delayed-time Absolute Dynamic Topography (ADT), Sea Level Anomalies (SLA) and Geostrophic surface currents which merges data from different altimeters (Taburet et al., 2019). The GW has a clear sea level signature and this data set has already been used in several previous studies to track its position (e.g., Beal & Donohue, 2013; Melzer et al., 2019; Trott et al., 2018). We use the Remote Sensing Systems merged infrared—microwave sea surface temperature (SST) data version 5.1 available from https://www.remss.com/ to

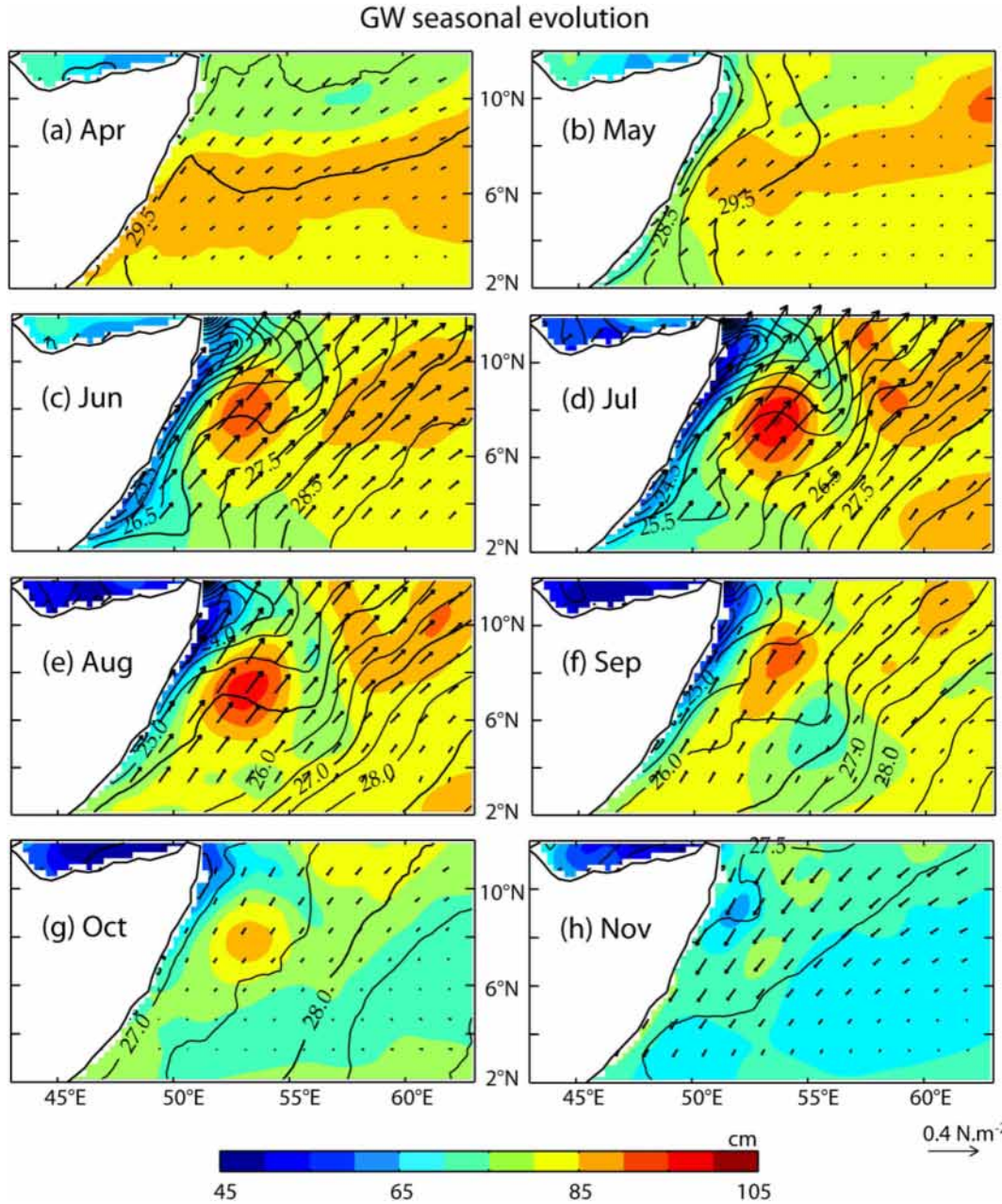

Figure 2. Observed (a–h) April to November monthly climatology (2003–2015) for Absolute Dynamic Topography (ADT; shading; cm), SST (contours; °C; 0.5°C intervals), and wind stress (vectors, $N.m^{-2}$).

describe the GW SST signature. The advantage of microwave data is that it provides measurements below clouds, which can be numerous in the region during the monsoon. Doing similar analyses using the merged infrared—in situ OISST v2 sea surface temperature (Reynolds et al., 2007) however provides very similar results (not shown). We document the GW signature on surface chlorophyll SChl using the ESA OC-CCI (Sathyendranath et al., 2018) data. In order to test the robustness of the link between wind stress forcing and the GW, we use several products: Tropflux (Praveen Kumar et al., 2013), ERA-I (Berrisford et al., 2011), and QSCAT (SeaPAC, 2013). The period used is indicated in the caption of each figure, but it is generally 1993–2015 for the purpose of analysis.

The intrinsic and wind-forced contribution to the total non-seasonal GW variability are derived from an ensemble of simulations performed with an ocean general circulation model (OGCM), which explicitly simulates non-linear

Table 1
Observational Data Sets Used in This Study

Data set	Spatial resolution (km)	Period considered	Description/Reference/Available at
DUACS DT18	25	1993–2016	Absolute Dynamic Topography (ADT), Sea level and Geostrophic surface currents Taburet et al. (2019) http://www.aviso.altimetry.fr/duacs/
OISST	25	1981–2016	Sea Surface Temperature Advanced Very High-Resolution Radiometer (AVHRR) V2 Reynolds et al. (2007) https://psl.noaa.gov/data/gridded/data.noaa.oisst.v2.highres.html
MW_IR OISST	9	2003–2016	Microwave and Infrared (MW_IR) Sea Surface TemperatureV5.1 Gentemann et al. (2010) https://www.remss.com/measurements/sea-surface-temperature/oisst-description/
OC-CCI	4	1998–2016	Surface Chlorophyll (SChl) from European Space Agency OC-CCI V3.1 Sathyendranath et al. (2018) http://esa-oceancolour-cci.org/
Tropflux	25	1972–2016	Wind stress Praveen Kumar et al. (2013) http://www.incois.gov.in/tropflux/
ERAI	25	1979–2016	ECMWF ERAI atmospheric reanalysis wind stress Berrisford et al. (2011) https://www.ecmwf.int/en/forecasts/dataset/ecmwf-reanalysis-interim
QSCAT	25	1999–2009	Wind stress SeaPAC (2013) https://climatedataguide.ucar.edu/climate-data/quikscat-near-sea-surface-wind-speed-and-direction

dynamics and the associated eddy variability. The analysis of a simulation performed with a linear, continuously-stratified (LCS) model further allows us to better understand the oceanic mechanisms leading to the wind-forced non-seasonal GW variability. Being linear, this LCS model does not produce any internally generated variability, but is useful to isolate the linear wind-forced oceanic response. Below, we detail each of those models.

The core of our modeling strategy relies on ocean simulations performed in the framework of the OceaniC Chaos - ImPacts strUcture predicTability (OCCIPUT) project (https://meom-group.github.io/projects/occiput; Bessières et al., 2017; Penduff et al., 2014). The main OCCIPUT ensemble is made of 50 global oceanic hindcasts based on the version 3.5 of Nucleus for European Modeling of the Ocean (NEMO; Madec, 2012), run over a 56 years period (1960–2015). This configuration is run in the eddy-permitting regime, at 1/4° horizontal resolution (~27 km at the equator, decreasing poleward) and 75 vertical levels. This is referred to as the "OCCIPUT ensemble" throughout the paper. It is forced using the DFS5.2 atmospheric forcing, which is based on ad-hoc corrections of the ECMWF ERA-interim re-analysis (Dussin et al., 2016). The model is first spun up from rest and climatological temperature and salinity data during 21 years, using first the climatological DFS5.2 forcing and then a progressive transition to the 1958–1960 DFS5.2 forcing (Leroux et al., 2018). During 1960, small random perturbations are introduced to each member's density equation in order to create dispersion within the ensemble (Bessières et al., 2017). These stochastic perturbations are only applied during 1960. They result in slightly different oceanic states at the beginning of 1961, mostly differing through different realizations of the meso-scale eddy field (e.g., Bessières et al., 2017). Apart from those different initial states at the beginning of 1961, each ensemble member is otherwise identical. In particular, those members share the identical DFS5.2 atmospheric forcing between 1961 and 2015 (Leroux et al., 2018). Differences between ensemble members over the period we analyze (in general 1993–2015) can hence only result from intrinsic oceanic variability such as that associated with the mesoscale-eddy field. The part of the variability that is common to all ensemble members (obtained through ensemble averaging) is on the other hand attributable to the common atmospheric forcing, which is common to all members.

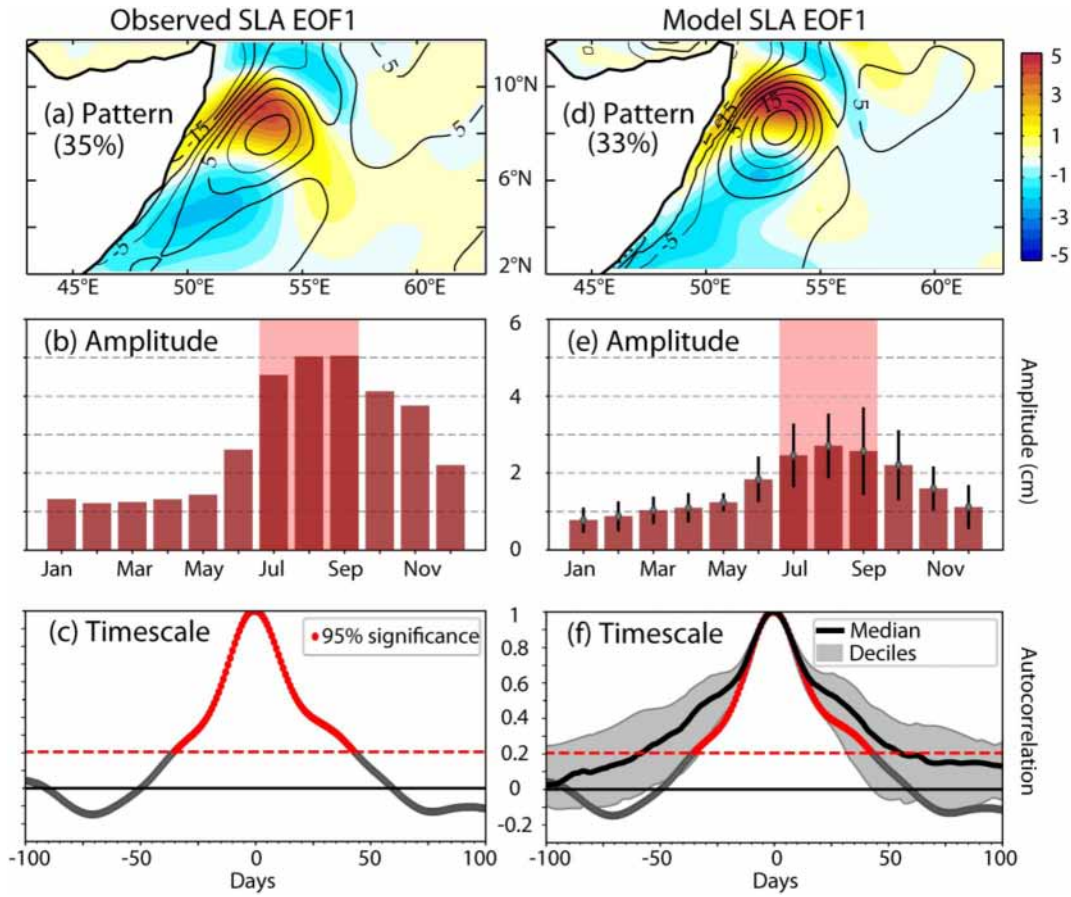

Figure 3. GW observed (left) and modeled (right) non-seasonal variability: (a) Spatial pattern of the first Empirical Orthogonal Function (EOF1; 35% of the total variance) of observed monthly sea level non-seasonal anomalies (SLA; the EOF have been normalized by their spatial standard deviation) during 1993–2015 for July, August, and September (JAS) marked as pink shading in bar plots. The JAS climatological absolute dynamic topography contours (interval 5 cm) are overlaid. (b) Seasonally stratified amplitude (cm) of the GWI or Great Whirl Index. The GWI is obtained by projecting the5-day SLA onto the normalized monthly SLA EOF1 displayed on panel a; refer to Section 2.2. The red shading highlights the J, A, S period over which the EOF have been computed. (c) Lagged autocorrelations of the daily interpolated GWI. On panel (c), correlations that are significantly different from zero at the 95% confidence level (using a *t*-test and assuming that each year is an independent sample) are displayed in red. (d–f) Same as (a–c) but for the OCCIPUT ensemble simulation. Panel (d) shows the EOF for one member of OCCIPUT (other members result in very similar patterns). The vertical bars on panel (e) and shading on panel (f) show the 10th and 90th percentiles (and the black line on f is the median). The observed autocorrelation curve from (c) has been replicated on panel (f) for an easier comparison.

Most of our results are obtained at a ¼° eddy-permitting resolution, but we also analyze a single-member interannual simulation at a 1/12° eddy-resolving horizontal resolution over 1966–2012 (47 years; performed under the Drakkar project using ORCA12 configuration with NEMO version 3.4. Details available at http://www.drakkar-ocean.eu.) in the discussion section, to assess the sensitivity of our results. The analyses in the entire paper are restricted to the common period with the DUACS Absolute Dynamic Topography (ADT) and Sea Level Anomalies (SLA) data sets (1993–2015, i.e. 23 years), but repeating the model analyses over the entire simulations length does not change the conclusions of our study (not shown).

In addition to our large-ensemble OGCM simulation approach, we also analyze a simulation performed with the linear, continuously stratified ocean model used in Suresh et al. (2013, 2016, 2018) and adapted from McCreary et al. (1996). The shallow water equations are solved individually for the first five vertical baroclinic modes, and the model solution is obtained as their sum. The model equations are discretized over a 0.25° resolution grid for the Indian Ocean domain (30°S–30°N, 30°E–110°E), with a coastline derived from the 200 m isobath. The model is forced with daily TropFlux wind-stress anomalies relative to the 1979–2015 long-term mean. This model

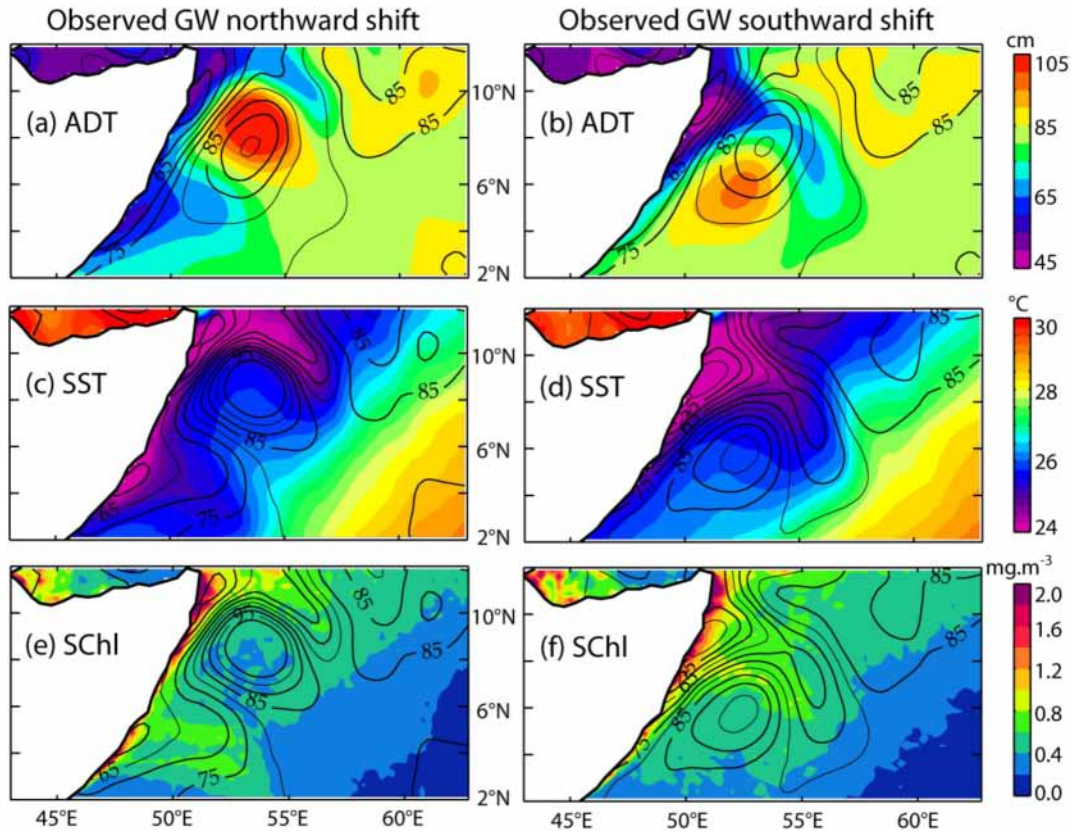

Figure 4. Observed composites of (left) northward and (right) southward GW shift events based on 5-day averages of the fields. The composites are built based on whether the, 5-day PC1, obtained by projection of 5-day SLA on to EOF1 of monthly SLA (refer to Section 2.2), is above or below 2/3 or below −2/3 of its standard deviation. (a, b) ADT (shading, cm) with the July–September climatological ADT as contours at 5-cm intervals, (c, d) SST (shading, °C), and (e, f) SChl (shading, mg.m^{-3}). In panels (c–f), the contours correspond to the ADT of the composite events displayed in panels (a) and (b), with 5-cm intervals.

accurately reproduces the Northern Indian Ocean response to wind variations at seasonal, intraseasonal and interannual timescales (Suresh et al., 2013, 2016, 2018). The linearity of the model prevents simulating mesoscale activity and more generally of intrinsic variability: this simulation will hence allow us to isolate the linear part of the ocean response to wind forcing.

2.2. Methods

All data sets are interpolated to a common 25-km resolution grid. Non-seasonal anomalies are constructed by removing the mean seasonal cycle over the 1993–2015 period and applying a linear detrending. The model sea level is drifting due to an unbalanced surface freshwater forcing: the domain-average sea-level is hence subtracted at each time step, and then adjusted to the mean observed value: this only matters for Figures 1, 2, 4, and 5 that show the total sea level, but does not influence the other figures based on sea level anomalies.

We use an empirical orthogonal function (EOF) analysis of the monthly sea level anomalies relative to the seasonal cycle over July, August and September and the [43ºE–62ºE, 2ºN–12ºN] domain, to isolate the leading mode of GW non-seasonal variations. The choice of this particular period of the year will be justified later, but the results are not extremely sensitive to adding 1 month before or after, or performing the analysis over the 3-months average (not shown). The main results of this study are also robust when changing a bit the domain boundaries or analysis period (1993–2015). We will see that the first EOF (EOF1) dominates the signal, and corresponds to a meridional displacement of the GW. Throughout the paper, we normalize the EOF1 by its spatial standard deviation, so that the corresponding PC1 has a unit in cm. The EOF analysis is performed on monthly averages, but the PC1 can be obtained at 5-day resolution through projection of the 5-day average SLA onto the normalized

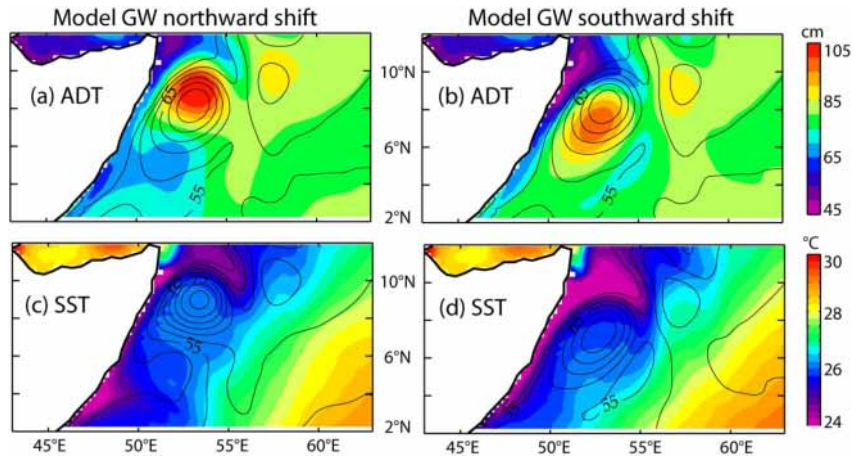

Figure 5. Same as ADT (a, b) and SST (c, d) composites based on the PC1 of sea level value as in observations, from an arbitrarily chosen single member of the OCCIPUT ensemble (other members result in very similar composites; not shown).

EOF1 pattern. Throughout the paper, we refer to this projection of the 5-day averaged SLA onto EOF1 as the "Great Whirl Index" or GWI. The reason why EOF are computed from monthly data and the PC re-projected (rather than computing directly the EOF from 5-day average data) will be clearer when discussing the results: eddies dominate at sub-monthly frequencies in the GW region, and the GW displacements only appear as the leading EOF at monthly or longer periods. By default, throughout the paper the "GWI" refers to the subseasonal GW index, at 5-day resolution, while the "seasonal GWI" refers to July–September average.

The forced (deterministic) and intrinsic (stochastic) contributions to the GW non-seasonal variations is isolated in our large ensemble simulation by following an approach similar to that in Leroux et al. (2018). Since the intrinsically generated signals are uncorrelated between members, computing the ensemble average across the 50 members will result in a ∼7-fold decrease in its amplitude. The ensemble average can thus be considered as a reasonable estimate of the externally forced signals (by the atmospheric forcing at the air-sea interface). Deviations between each member and the ensemble mean allows evaluating 50 different realizations of the intrinsic variability contribution. If we note η_i the sea-level of the ith ensemble member and $< >$ the ensemble average, then $\eta = <\eta_i>$ is our estimate of the deterministic response to atmospheric forcing and $\eta'_i = \eta_i - <\eta>$ our 50 realizations of the intrinsic variability (in particular mesoscale oceanic eddies). Statistics such as the variance of the intrinsic variability are quite similar from member to member when computed over our 23-year long reference period, but we display ensemble mean statistics for more robustness.

3. Observed Non-Seasonal Variability of the GW

Here, we first recall the seasonal lifecycle of the GW before studying its non-seasonal variability. Figure 2 displays the mean seasonal cycle of the ADT (shading), wind stress (vectors) and SST (contours) from April to November. In April (Figure 2a), the ADT shows a maximum around 6–8°N band, associated with the annual Rossby wave that is radiated westward from the west coast of India (Shankar & Shetye, 1997). Weak southwesterlies appear in May (Figure 2b) and induce a weak coastal upwelling signal, visible as a band of lower SST and ADT along the Somalia coast. At this time, an anticyclonic oceanic circulation that prefigures the GW appears at about 8°N, aligned with the sea level maximum associated with the annual Rossby wave, as pointed out by Beal and Donohue (2013). Although appearing on average in April (Beal & Donohue, 2013), the GW becomes most clear on Figure 2 in June, along with the Findlatter jet onset and a strong coastal upwelling signal, and contributes to the splitting of the coastal upwelling into two cold wedges during June, July and August (Figures 2c, 2d, and 2e). The GW is the strongest in July, decays thereafter (Figures 2e, 2f, and 2g) and disappears completely in November (Figure 2h). This description is consistent with most recent studies (e.g., Beal & Donohue, 2013; Cao & Hu, 2015; Melzer et al., 2019; Trott et al., 2018; Wang et al., 2019). The climatological GW is fully developed and stable in its shape and position during the June, July, August period.

As in most previous studies, we use sea level to describe the GW. We perform an EOF analysis on non-seasonal sea level anomalies to characterize the GW non-seasonal variability. As will be explained later, the non-

seasonal variability is maximum during the period from July to September, and we hence performed the EOF analysis over this seasonal window. The leading EOF (EOF1) of observed, non-seasonal monthly SLA in the GW region for July, August and September is a north-south dipole pattern (Figure 3a), which explains about one third (35%) of the total non-seasonal SLA variance in this region. The nodal region of this SLA dipolar structure is centered on the mean GW central latitude (7–8°N, see Figure 2d), with positive values to the north (7–10°N) and negative to the south (3–7°N). This SLA pattern hence describes a meridional shift of the GW location from its climatological position (northward shift for positive PC1 values, and southward shift for negative ones). We will confirm this a bit later using a composite analysis. The higher order EOFs (other than the leading mode) explain less than 20% of the total variance and will not be discussed in the following.

Figure 3b shows the seasonal cycle of the 5-day GWI (Great Whirl Index) amplitude. We remind that the GWI (in cm) is defined as the projection of 5-day sea level anomalies relative to the seasonal cycle onto the normalized EOF1, and encodes information about the amplitude of the GW meridional displacement. The GWI is more variable during June–December, and maximum between July to September. This justifies our choice of the period to define the main pattern of non-seasonal variability. Figure 3c shows the lagged autocorrelation of the GWI (obtained at daily intervals through interpolation of the 5-day data), which allows us to estimate the typical timescales of the GW meridional shifts. The autocorrelation curve shows a central lobe, with a fast decrease in correlation at about ±15 days lag, indicating a fast timescale of ∼30 days. The lagged autocorrelation then decays more slowly, and becomes undiscernible from zero at the 95% confidence level (about 0.2) within 35–40 days, suggesting a second, slower timescale for typical GW shift events of 70–80 days.

As discussed above, the normalized GWI (i.e., the 5-day PC1, normalized by its standard deviation) characterizes the non-seasonal variability in the GW central latitude. We thus obtain composites of northward-displaced GW based on GWI values above 2/3 (see Figure 4a) and of southward-displaced GW based on GWI values below −2/3 (see Figure 4b). The former are characterized by a stronger than usual GW (compare the ADT values shaded vs. contour on Figure 4a), that is shifted ∼100 km northward relative to its climatological position (Figure 4a). The latter correspond to weaker than usual GW, that is shifted ∼200 km southward relative to its climatological position (Figure 4b). In the observations, the amplitude of the GW meridional shifts is about 30 km per cm of GWI. Because of these fast meridional oscillations, the GW appears to be meridionally broader on the ADT climatology than while considering those composites or snapshots (compare the colors and contours on Figures 4a and 4b). Those GW meridional shifts are also associated with clear changes in the coastal sea level, and hence coastal upwelling: two negative coastal SLA wedges are clearly visible at 5°N and 10°N when the GW is anomalously shifted northward, but the southern wedge is suppressed and the northern wedge intensified in the case of a southward shift (Figures 4a and 4b). This modulation is likely associated with the GW-induced mass transport. This transport is shoreward and suppresses the coastal upwelling on the GW southward flank, and vice-versa on its northward flank.

As discussed in the introduction and above, the GW strongly modulates the structure of the coastal upwelling, and the lateral export of cold, nutrient-rich waters from this upwelling area toward the central Arabian Sea. Figures 4c–4f shows similar composites to those in Figures 4a and 4b, but for SST and SChl. In general, the GW corresponds to an anticyclone associated with warmer and less productive waters compared to its surrounding environment. The SST and SChl coastal signature and its offshore extension displays marked contrasts between situations with a northward- and southward-shifted GW. As with SLA, the GW northward shift is associated with two well-defined coastal cold and productive wedges centered around 5°N and 10°N extending offshore (Figures 4c and 4e). On the other hand, a GW southward shift is related to a suppression of the cold and productive wedge at 5°N, and a stronger-than-usual cold, productive wedge at 10°N (Figures 4d and 4f). These results indicate that the GW non-seasonal variability that we have isolated in observations has a strong impact on the physical and biogeochemical characteristics in the coastal and offshore regions near Somalia.

Overall, in this section, we have demonstrated that the main mode of observed non-seasonal GW variations is associated with ∼100 km northward or southward shifts, with energetic variations in the 30–80 days window. The GW is intensified when shifted northward, and there are two clear cold and productive wedges at 5°N and 10°N. The GW is weakened when shifted south, the southern wedge disappears and the northern wedge intensifies.

4. Intrinsic and Forced GW Variability in the Ensemble Simulation

In this section, we will first verify that the model reasonably reproduces the observed non-seasonal variability of the GW (Section 4.1). We will then characterize the pattern, amplitude, timescales and seasonality of the internally generated and forced parts of the GW variability (Section 4.2). We will then show that the intrinsic variability of the GW is intraseasonal, and related to interactions with mesoscale eddies, as outlined by Beal and Donohue (2013) (Section 4.3). Then we will show that the GW forced seasonal-mean response is the result of a shift in the probabilities of the intraseasonally varying GW position (Section 4.4). Finally, we will discuss potential mechanisms of the GW forced response, and its links with large-scale climate modes (Section 4.5).

4.1. Modeled GW Non-Seasonal Variability

Overall, the mean state and seasonal cycle of the GW are reasonably well simulated by the model (comparable to Figure 2; not shown). Figures 3d–3f provides EOF analyses from the model similar to those in Figures 3a–3c for the observations. The EOF of Figure 3d is shown for a particular member, but other members display very similar patterns (not shown). The other analyses were performed for all members, and the median and 10th–90th percentiles are both displayed to illustrate uncertainties on the statistics of this mode due to intrinsic variability. The main features of the non-seasonal GW variations in the OCCIPUT ensemble are similar to those in observations. First, the leading EOF pattern is characterized by a north-south SLA dipole (Figure 3d) and the explained variance (33%) is similar to that in observations (35%). Second, the seasonality of the GW index (meridional movements amplitude) is strongest during July–September as in observations (Figures 3e vs. 3b). Finally, the autocorrelation curve has a similar shape to that in observations (Figures 3f vs. 3e), with a central lobe indicating a first timescale of ∼30 days and a lower-frequency second timescale of about 100 days, slightly longer than in observations. The 10th–90th percentile indicates, however, that intrinsic variability induces significant uncertainty on this autocorrelation statistic, leading to an observed curve that is almost often within the bounds of the model estimates. Despite this broad agreement, the modeled GW index is about half as variable as in observations, which lie outside of the model 10–90% confidence interval (compare Figures 3b and 3e). The underestimation of the range of the GW meridional displacements by about 30% (Figure 3e) in our model is discussed in Section 5.2.

Figure 5 examines whether the aforementioned non-seasonal variability in modeled SLA is associated with SST signals similar to those in observations (Figure 4). The lack of a biogeochemical component in OCCIPUT simulations does not allow us to evaluate the modeled response in SChl. The composites in Figure 5 are constructed as in observations, based on GWI values above or below + or −2/3 standard deviation, for an arbitrarily chosen ensemble member of OCCIPUT (other members yield very similar composites; not shown). The modeled non-seasonal displacements in the GW are consistent with the observed characteristics. During northward shifts, the GW is more intense and splits the coastal upwelling into two coastal cold wedges around 4°N (vs. 5°N in observations) and 10°N (Figures 5a and 5c). During southward shifts, the GW is less intense, the southern cold wedge almost disappears, while the northern cold wedge intensifies (Figures 5b and 5d). Figures 4 and 5 composites indicate a displacement amplitude of ∼200 km in the model (100 km northward and southward), and ∼300 km in observations (∼100 km northward and ∼200 km southward). The GW displacement amplitude is thus ∼30% smaller in the model than observed.

This section thus demonstrates that the GW in the OCCIPUT simulations has a seasonal cycle similar to that in observations. It also has very similar non-seasonal characteristics in terms of temporal scales, spatial pattern and seasonality, the main bias being that the amplitude of the modeled GW meridional shifts is about one third smaller than that in observations. The modeled GW shifts also have qualitatively similar SST signatures to those in observations, with two cold wedges at 4°N and 10°N when the GW is shifted northward and stronger, and a single intensified cold wedge at 10°N when the GW is shifted southward and weaker. This agreement is sufficient to allow us to address the question in the next section: how much of the GW variability is intrinsically generated, and how much can be related to external forcing?

4.2. Intrinsic and Forced GW Variability Properties

Figures 6a and 6b shows the EOF1 of monthly SLA anomalies in summer separately for the forced and intrinsic components (see Section 2.2 and figure caption for methodological details on how to separate these two contributions). The leading EOFs for both components display nearly identical spatial patterns, similar to that in observations (Figure 3a). This indicates that the sea level signals resulting from intrinsic and forced variability are

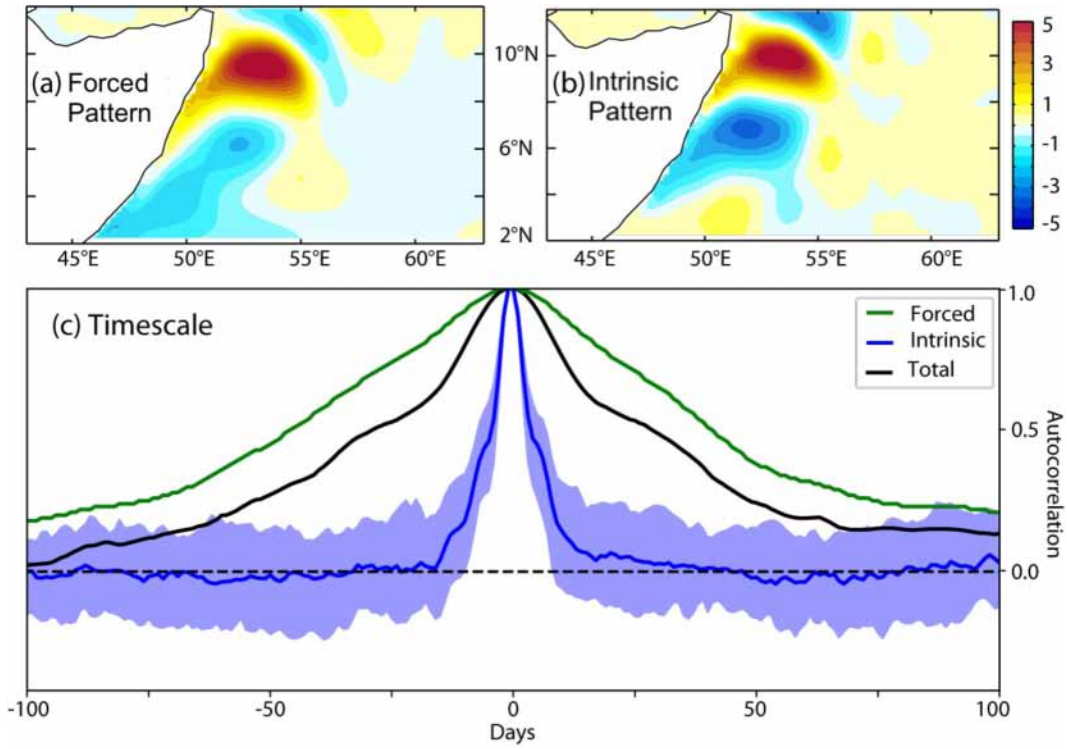

Figure 6. Spatial patterns of the leading EOF mode of the monthly July, August, and September non-seasonal sea level anomalies SLA (cm) (normalized by their respective spatial standard deviation) for (a) forced signals (ensemble mean of OCCIPUT), and (b) internal variability (same member as Figure 5 minus the ensemble mean, see Section 2.2; other members result in a very similar pattern). (c) Lagged autocorrelations of the Great Whirl Index (GWI) for the forced (green), total (median of the ensemble, black), and intrinsic (median of the ensemble in blue, and 10th–90th percentile as shading) components. Daily GWI time series are obtained by interpolating the 5-day GWI to daily values.

both dominated by northward or southward GW shifts in this region. Figure 6c shows the lagged PC autocorrelation associated with total variability (black curve, same curve as on 3f), and its forced (green) and intrinsic (blue for the ensemble median) components. The forced response clearly exhibits a much longer timescale than the intrinsic response, with a typical event duration of ∼100 days (assuming exponential decay). The intrinsic variability has a much shorter timescale, on the order of 20–25 days. It is very likely that it is the combination of those two timescales that produces the short and long timescales in the lagged autocorrelation of the total (forced + intrinsic) signal in the model (black curve) and observations (Figure 3f). Overall, the deterministic response of the GW has a longer timescale but the same spatial pattern as that of the intrinsic variability, which may seem surprising. This is in fact quite a typical feature in chaotic systems such as the atmosphere (Palmer, 1999) (or here the ocean at mesoscale), and we will discuss how it can be explained in Section 4.3.

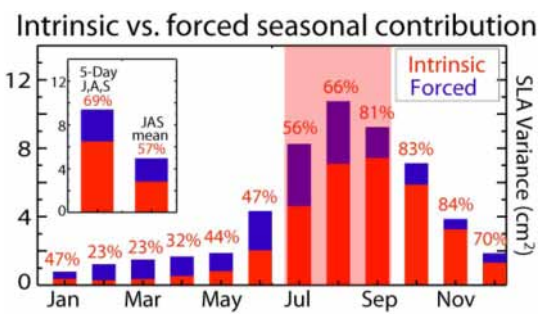

Figure 7. Seasonally stratified amplitude of the Great Whirl Index (GWI) in the OCCIPUT ensemble, with contributions from the intrinsic (red) and forced (blue) parts. The % of intrinsic contribution to the total variability is indicated above each bar. This estimate is computed from the 5-day GWI. The pink shading highlights the period of largest GW non-seasonal variability (July to September). The inset compares the % of intrinsic (red) and forced (blue) contributions for the 5-day GWI over July, August and September and the July–September average GWI.

Figure 7 shows the intrinsic and forced contributions to the GWI (i.e., to the GW meridional shifts) and its seasonality. We remind that the GWI is based on pentad data, in order to fully resolve the short timescale associated with the GW intrinsic variability. The forced and intrinsic components contribute almost equally to the GW meridional movements early in the summer season (56% intrinsic contribution in July), but the intrinsic contribution takes over later (81% in September, and even more in October when the GW usually dissipates Figure 2). The inset shows that the intrinsic contribution to the 5-day GWI over July, August and September is 69%. The other bar plot in the inset gives the intrinsic and forced contributions for the seasonally (July to September) averaged GWI. The intrinsic contribution should decrease when

averaging seasonally (typically by a factor of 2 if we consider one degree of freedom per 20-day), relative to the forced contribution that has a longer timescale (about one sample per season). We hence expect a larger contribution of the forced variability at the seasonal timescale. The inset confirms that this is the case but that intrinsic variability still dominates, with a 57% contribution of intrinsic variations and 43% contribution of forced signals to the seasonal mean GWI.

Overall, this section shows that the deterministic response is associated with forced variability that typically lasts for a season, while intrinsic variability has a much shorter ∼20 days time scale. Intrinsic GW meridional shifts are dominant at intraseasonal timescales (66% over July–September, with highest contributions in September), and for seasonal averages, albeit with a weaker contribution (57%) in the latter case. In the following section, we propose some clues for the GW intraseasonal intrinsic displacements mechanism.

4.3. Intrinsic Intraseasonal Modulation of the GW

Previous studies have underlined that the GW is a strongly nonlinear phenomenon (e.g., Beal & Donohue, 2013; Fischer et al., 1996; Knox & Anderson, 1985). It may thus display self-sustained oscillations without the need for interactions with another phenomenon. Beal and Donohue (2013) however showed that the intraseasonal modulation of the GW was associated with a clear interaction with nearby mesoscale eddies. Because the meso-scale eddy field is inherently the result of intrinsic ocean instabilities, it is also a relevant candidate to explain the intrinsic GW signals. In this section, we explore the GW interaction with the meso-scale eddy field in the OCCIPUT ensemble.

The spatial structure of the EOF associated with the GW movements has been obtained from monthly averaged SLA, which has less meso-scale eddies signature than 5-day fields, and thus allows the GW displacement to emerge as the lead EOF. Figure 8c shows the EOF pattern of the 5-day intrinsic component of sea level anomalies: the pattern from this higher-frequency analysis clearly differs from that of the monthly EOF analysis (Figure 6b), indicating that it does not describe GW meridional shifts but rather four meso-scale eddies of alternating signs around the central position of the GW. A lead-lag regression on the associated PC indicates that those eddies tend to rotate clockwise around the GW, probably in relation to advection by GW currents. This is a very similar picture to that described by Beal and Donohue (2013) from sea level snapshots.

Figure 8f shows the average of Figure 8 panels a, b, c, d and e, that is, a 20-day average of the leading mode of high-frequency intrinsic variability of SLA in the region. This analysis reveals that the residual of the eddy movements over 20 days has a very similar pattern to that of the intrinsic variability on Figure 6b (pattern correlation of 0.94). This suggests that the interaction with the nearby meso-scale eddies is the primary source of intraseasonal meridional shifts of the GW, typically lasting 20 days or less, as proposed by Beal and Donohue (2013). The detailed mechanism of this intrinsic variability resulting from interaction with mesoscale eddies, however, is still not yet clear: we will return to this in the discussion.

The western Arabian Sea displays an intense oceanic eddy activity during the monsoon, mainly due to barotropic instabilities in the intense Somalia current and baroclinic instabilities at the oceanward edge of the coastal upwelling (Vic et al., 2017; Zhan et al., 2020). This section suggests that the intrinsic variability of the GW (with a typical duration of ∼20 days) is due to its interaction with this intense mesoscale eddy field, as first suggested by Beal and Donohue (2013). In the following section, we will investigate the forced component of the variability, which is associated with longer timescales (∼100 days duration), that is, seasonal signals.

4.4. Forced GW Signals as a Shift of the Intrinsic Variability Probability Distribution

Above, we saw that the intrinsic GW meridional displacements have a ∼20 days (intraseasonal) timescale which results from the interaction between the GW and neighboring mesoscale eddies. The GW meridional movements arise from the interaction with a turbulent field that is likely in the chaotic regime. It may hence sound surprising that they could exhibit a forced response at a lower frequency (typically at a 100-day timescale). It may seem even more surprising that this forced response has the same spatial pattern as the intrinsic variability. In fact, this is not an atypical situation, in chaotic systems such as the atmosphere. The Pacific North-Atlantic (PNA) pattern, for example, is a reproducible atmospheric pattern over the North Pacific and North America, that displays energetic, high-frequency intrinsic fluctuations, but that also clearly shows a forced variability in response to ENSO on interannual timescales (e.g., Feldstein, 2000). Palmer (1999) illustrated how forcing acts in a chaotic system using

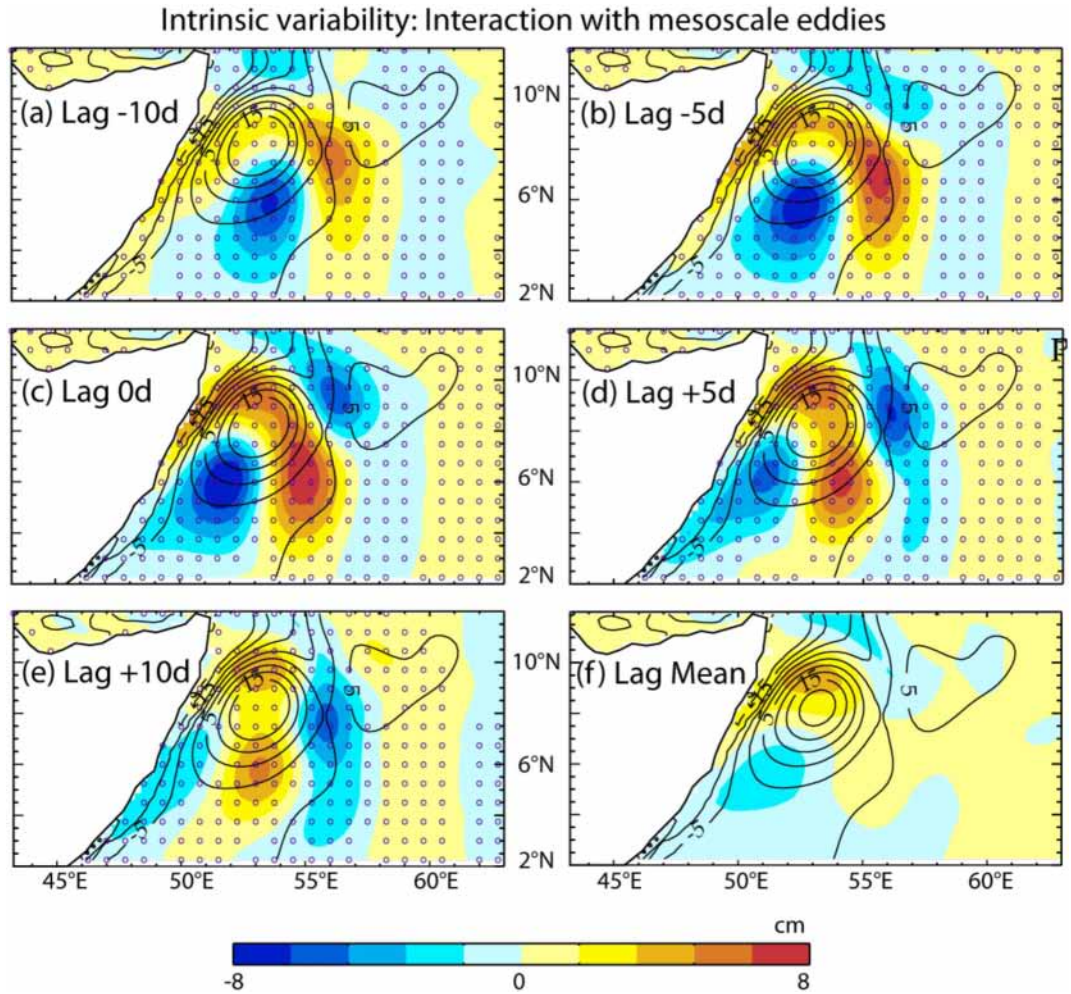

Figure 8. (a–e) The sea level non-seasonal anomalies (SLA) spatial pattern (cm) obtained from a lead-lag regression of the intrinsic (single member minus the ensemble mean) component onto normalized 5-day intrinsic Great Whirl Index (GWI); (f) the mean pattern obtained by averaging the sea level patterns shown in panels (a–e). Contours indicate the climatological July–September sea level in the model, to highlight the GW mean position. The circles indicate regression significantly different from zero at the 95% confidence level.

a simple analog in the Lorenz (1963) model. Forcing that projects on the spatial pattern of an intrinsic mode of variability of the system may simply modify its probability distribution. The system will remain highly variable, but the slightly shifted probability density will result in a forced response when averaged over time. We show below that the GW meridional displacements forced response is indeed associated with shifts in the probability density of the intrinsic variability, explaining why the forced response and intrinsic variability have the same pattern, but different timescales.

Figure 9a shows the seasonal (July to September) mean GWI from the OCCIPUT ensemble, with the black line indicating the ensemble mean (forced signal) and the light gray shading displaying the 10th and 90th percentiles of its probability distribution. Red stars indicate years when the seasonal mean GWI value is above 2/3 standard deviations and blue circles years below −2/3. Most extreme years correspond to seasonal mean GW index values of 2–3 cm, which typically corresponds to 50–75 km meridional shifts in the model. Although there is a forced signal, there is still a considerable random component to the seasonal-mean GWI. There is indeed not a single year when the entire probability distribution is shifted to positive or negative values, even in the cases of most extreme positive (1998, 2005) or negative (1999, 2008) PC values. Figures 9b and 9c illustrates the even larger spread at subseasonal timescales for the years with the most positive (1998) and most negative signals (1999). It shows that

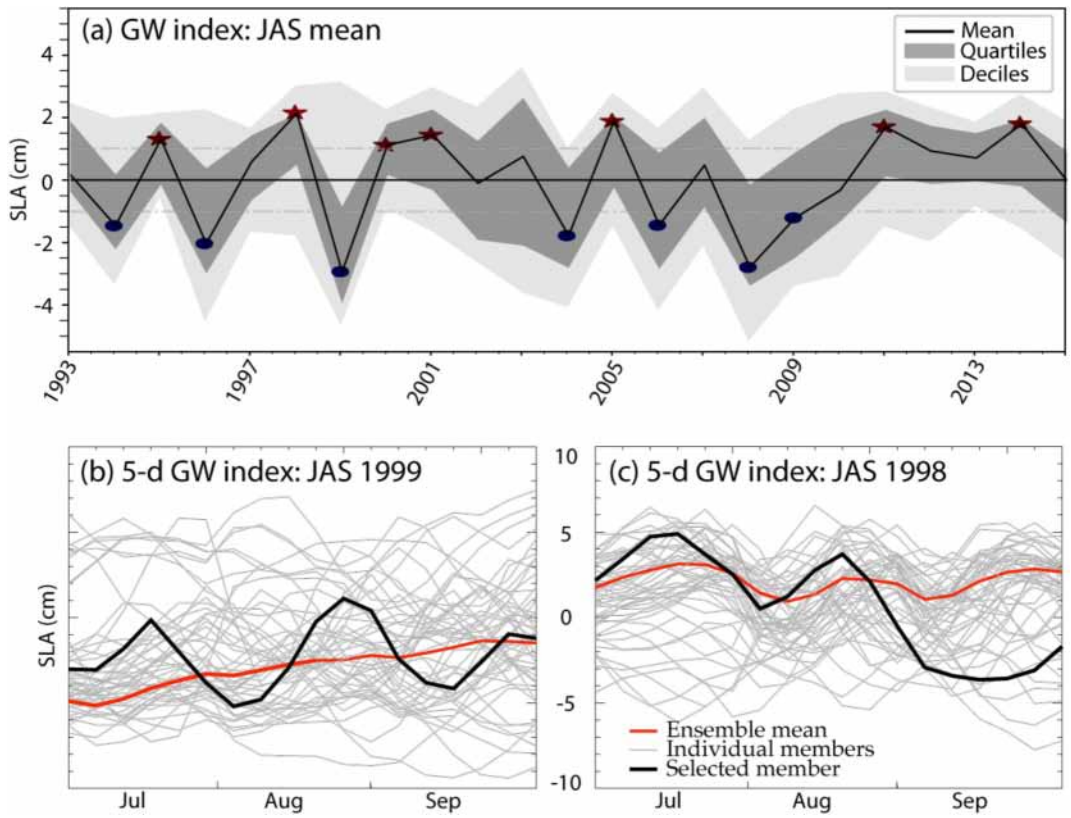

Figure 9. (a) Time series of the average July – September GWI (Great Whirl Index) in the OCCIPUT ensemble: forced contribution (ensemble mean, black) and 10th–90th percentiles (gray shading). Red stars denote years with an unusually high GWI (northward-shifted GW) forced signal (forced JAS GWI > 2/3 standard deviations). Blue circles denote years with an unusually low GWI (southward-shifted GW) forced signal (forced JAS GWI < −2/3 standard deviations). (b, c) Time series of July–September 5-day GWI for negative (1999) and positive (1998) year for individual members (gray lines), ensemble mean (red) and randomly selected member (black).

years with, for example, a seasonally averaged northward shifted GW have both occurrences of northward- and southward-shifted GW, alternating at subseasonal scales.

Figure 9 suggests that the forced seasonal mean signal (black curve) results from shifts of the entire distribution. This is particularly clear for the 90th percentile of the distribution, which has a 0.87 correlation with the ensemble mean (forced signal), somewhat less so for the tenth percentile (0.46 correlation, which is still different from zero at the 95% confidence level). Figure 10a shows a composite probability density function of the 5-day GWI for years when this forced seasonal (July to September)-mean index is anomalously high/low (red stars and blue circles on Figure 9a, respectively). This figure clearly indicates that the forced seasonal-mean signal is associated with shifts in the entire subseasonal GWI probability distribution. In other words, a forced signal is not associated with a GW that is always shifted northward, but with a more likely shift northward than southward. The GW intrinsic variability in our model is in principle completely uncorrelated with that of the observations. On the other hand, the model forced variability should, to some extent, reproduce the forced variability of the observations (and should reproduce it perfectly in the hypothetical perfect model limit). To test this assumption, we analyze whether the probability density function of the subseasonal GWI in observations is also shifted conditioned to the modeled seasonal-mean forced signal (stars and circles on Figure 9a). Figure 10b indicates that this is the case: a seasonal-mean forced GW northward (southward) shift in the model corresponds to a more likely northward (southward) shift of the GW in observations. This powerful test highlights the model's ability to reproduce the forced GW signals and its mechanisms and confirms that the forced signal at the seasonal timescale is associated with a modulation of the intrinsic subseasonal GW variability.

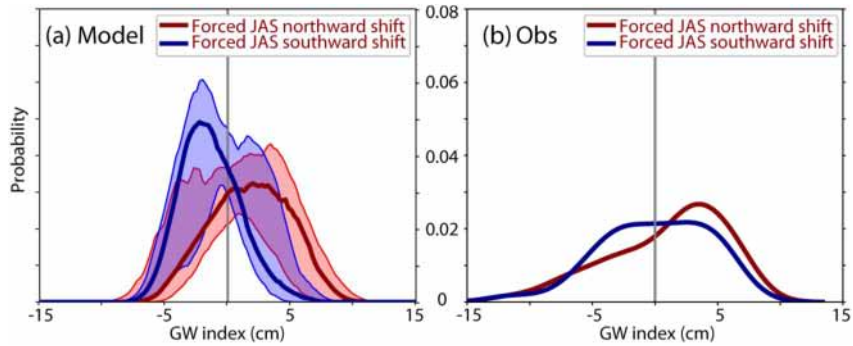

Figure 10. Probability density distribution of the July, August, and September 5-day Great Whirl Index (GWI) for (in red) years with a forced northward-shift of the GW (red stars on Figure 9) and (in blue) years with a forced southward-shift of the GW (blue circles on Figure 9). Those probability distributions are displayed for (a) the 50 members of the OCCIPUT ensemble (median distribution as a thick line, and 10th–90th interval as a shading) and (b) observations.

In this section, we have shown that the seasonally averaged forced signal is the result of a shift in the probability distribution of the subseasonal intrinsic variability, as is often the case in chaotic systems (e.g., Palmer, 1999). This explains why the forced contribution has the same spatial pattern as the intrinsic contribution. The GW intrinsic variability is reduced when averaging seasonally, but still a bit larger than the forced contribution (57% of the variance).

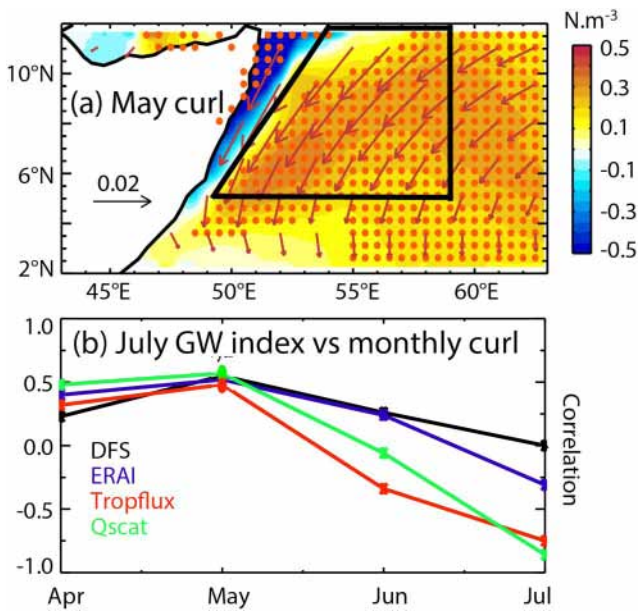

Figure 11. (a) Patterns of May wind stress (vectors; $N.m^{-2}$) and wind stress curl (shading; $N.m^{-3}$), obtained by regression on the normalized forced (i.e., ensemble mean) July monthly average Great Whirl Index (GWI). Red dots indicate wind stress curl signals that are significantly different from zero at the 95% confidence level. (b) Correlation of July monthly average GWI with the monthly (April to July) offshore wind-stress curl averaged within the black frame on panel a from DFS, for the ERAI, Tropflux, and QuikSCAT wind products. Correlations are significant at 95% for DFS, Tropflux and ERAI, and 80% for QuikSCAT.

4.5. Forced GW Shifts Mechanism and Potential Link With Large-Scale Climate Modes

This section is more exploratory than the rest of the paper. It aims to formulate a mechanism hypothesis explaining the forced contribution to the GW meridional shifts. Previous studies have suggested that Rossby Waves emanating from the west coast of India or forced east of the GW may play a role in its seasonal development (e.g., Beal & Donohue, 2013; Vic et al., 2014). We searched for wind and SLA precursors to non-seasonal GW shifts by regressing the non-seasonal wind and SLA signals during the first half of the year to the average July OCCIPUT forced GWI (we focus on July, as it has the largest forced component: Figure 7). Figure 11a displays the largest amplitude and most significant wind precursor we isolated. This precursor is a northeasterly wind anomaly that occurs in May, associated with a positive wind stress curl over a wide offshore region. Figure 11b tests the sensitivity of this wind stress curl precursor to the wind products. The lead correlation ($r \sim 0.5$) of the May average wind stress curl over the black frame on Figure 11a to the July average GW index is different from zero at the 95% confidence level for all the wind products we considered. The May wind-stress curl off Somalia hence appears to be a precursor to the forced non-seasonal meridional GW shifts.

Figure 12 shows lag-regressions of the observed and OCCIPUT forced SLA to the aforementioned wind stress curl precursor. The May northeasterly anomaly induces statistically significant anomalous downwelling along the coast in the model and observations (Figures 12a and 12d). The associated positive offshore curl tends to induce upwelling offshore in both the model and observations (Figures 12a and 12d). This zonal SLA dipole evolves into a meridional dipole in June (Figures 12b and 12e), but remains rather weak (typically a few cm). It is only in July that the signal amplifies strongly to become a north-south dipole characteristic of the anomalous northward GW shift and intensification (Figures 12c and 12f). This analysis hence indicates

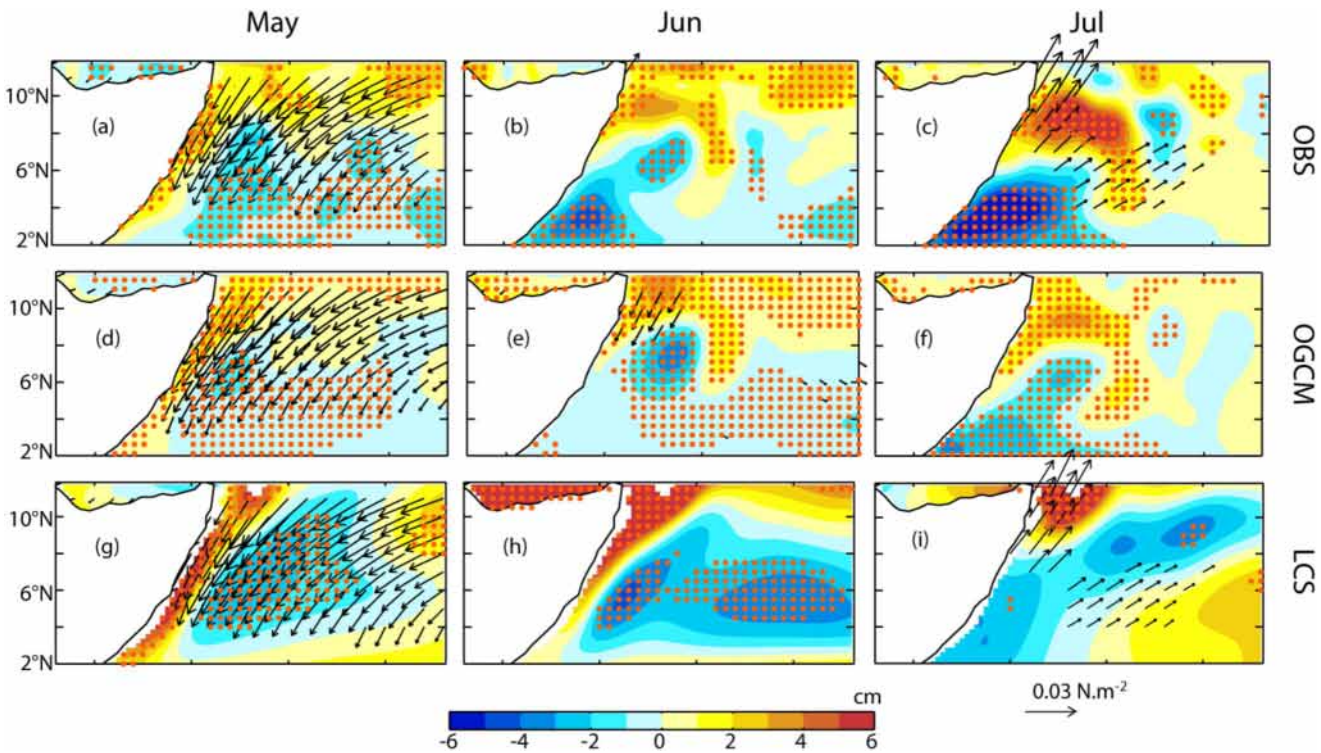

Figure 12. Spatial patterns of the May, June, and July SLA (colors) and wind stress (vectors), obtained by lag regression on the normalized May average wind stress curl within the black frame on Figure 11a from (a, b, c) observations (Tropflux for wind stress), (d, e, f) OGCM that is, OCCIPUT ensemble mean and (g, h, i) LCS the linear-continuously stratified ocean model. Red dots indicate SLA signals that are different from zero at the 90% confidence level, and only wind stresses that are significant at the 85% confidence level are plotted. The SLA from the linear model simulation is scaled by a factor of 5 to enable comparison with other panels.

that the May wind pattern is the driver of an east-west SLA dipole in May that evolves into the stronger north-south SLA dipole that characterizes GW meridional shifts in July.

To assess whether this evolution from a zonal to a meridional dipole is consistent with linear dynamics, a similar analysis is performed in a linear model (see Section 2). As in observations and in the non-linear ocean model, the May wind stress precursor acts to deepen the thermocline along the coast and shoals it further offshore. The evolution of the LCS model SLA signal during the following months shares similarities with that in observations and the non-linear model. This suggest that the formation of a north-south SLA dipole near the Somalian coast in July, can result from the linear response to northeasterly wind anomaly in May. We suggest that it is associated with the faster propagation of Rossby waves at 4°N (about 0.8 m/s for the first baroclinic mode) than at 8°N (about 0.35 m/s), although higher order baroclinic modes and reflection into short Rossby waves at the western boundary may also be involved. This linear response has a meridional dipole structure in June–July, that projects onto that of the GW intrinsic variability. It may hence act as a persistent forcing of the GW nonlinear dynamics at the seasonal timescale, that acts to favor more likely phases of one polarity of the GW shifts, as was discussed in the previous section.

The above analysis proposes a plausible mechanism by which a specific wind pattern in May could contribute to forcing non-seasonal meridional GW shifts during the summer. However, it is not clear whether this wind pattern is related to a known climate mode, such as ENSO in the Pacific or the IOD in the Indian Ocean, to random atmospheric variability, or to intraseasonal wind modulation associated with the monsoon onset (e.g., Goswami, 2005). The highest correlation we found between the May offshore wind-stress curl and a climate index is for the previous El Niño peak (0.43, different from zero at the 95% confidence level). ENSO indeed induces a delayed climate response in the Indian Ocean, with local air-sea interactions favoring wind and SST changes in the north Indian Ocean during the following spring (Du et al., 2009; Izumo et al., 2008; Xie et al., 2009). It is thus possible that ENSO has a remote influence on the forced response of the GW, although the correlation and thus the variance explained is rather low, indicating that other wind fluctuations in the southern Arabian Sea (linked to

other climate modes, intraseasonal variability or random) probably also contribute to generating Rossby Waves that influence the GW.

5. Summary and Discussion

5.1. Summary

The Great Whirl is a quasi-permanent anticyclonic eddy that forms on average in June and dissipates in October, off the Somalia upwelling. The GW plays an important role in exchanges of heat and biogeochemical properties between the coastal upwelling and open ocean. While the GW seasonal cycle has been widely studied, deviations from this mean seasonal cycle (hereafter, non-seasonal anomalies) have been less investigated. In this paper, we analyze the pattern and timescales of this non-seasonal variability from satellite observations. We also use the OCCIPUT 25-km resolution ocean general circulation model ensemble simulation to explore the relative roles of internal oceanic variability and external forcing in this GW non-seasonal variability.

Satellite observations indicate that the leading EOF of monthly sea-level anomalies in the region (35% of the total variance, with the following EOF explaining less than 20%) is associated with a north-south dipole centered on the mean GW position. We define a 5-day GWI (GW index) by projecting 5-day mean sea-level anomalies onto this normalized EOF1: this index describes displacements of about 30 km/cm of GWI. Composite analyses of satellite sea level, sea surface temperature and surface chlorophyll indicate that typical ∼100 km northward GW shifts are associated with a stronger GW, and two cold, productive coastal upwelling wedges at 5 and 10°N. Typical ∼200 km southward GW shifts are associated with a weaker GW, no wedge at 5°N and a single stronger-than-usual cold and productive wedge at 10°N. The GWI lagged-autocorrelation indicates a fast, subseasonal variability and a slower ∼100 days timescale.

The OCCIPUT ensemble simulation reproduces all of the above physical features fairly well, despite some underestimation of the GW southward displacements in the model. The ensemble approach allows separating the meridional GW movements into an internally generated and a forced part. This approach indicates that the GWI has a ∼20 days timescale intrinsic component, associated with the GW interaction with neighboring mesoscale eddies, a subseasonal GW variability that has been previously highlighted by Beal and Donohue (2013). The slower component of the modeled GWI is associated with a lower-frequency, ∼100 days externally forced component. Intrinsic variability dominates the GWI at both subseasonal timescales (67% of the variance over July, August, September and up to 83% for September) and at seasonal timescales (57% of the variance). The external forcing is associated with shifts in the subseasonal GWI distributions. That is, a year with a forced northward-shifted GW response has alternating northward and southward shifted GW situations with a typical 20-day timescale, but more likely northward than southward shifts. The observed GWI density distribution quite remarkably exhibits similar shifts when conditioned to the modeled forced seasonal mean GWI, suggesting that the external forcing identified in the model also operates in nature. The exact mechanisms of this external forcing, however, remain unclear. The model forced response in July is significantly associated with an offshore wind stress curl signal in May. The model forced response, observations and a linear model indicate that the linear response to this wind pattern is initially associated with an east-west sea level dipole, which evolves into a north-south dipole that projects onto the leading pattern of GW variability in July. The exact mechanism of this forcing, and its possible drivers (a climate mode such as ENSO or the IOD; interannual or intraseasonal modulation of the monsoon; random atmospheric variability or all of those?) will need to be investigated further in the future.

5.2. Discussion

Many previous studies have identified non-seasonal GW signals (Beal & Donohue, 2013; Cao & Hu, 2015; Melzer et al., 2019; Trott et al., 2018; Wang et al., 2019). The added value of our study is to document that these non-seasonal variations are more specifically associated with meridional shifts in the GW (for which we define an index), and that those meridional shifts are accompanied by clear SST and surface Chl signals, and in particular by a modulation of the two cold and productive SST wedges of the Somalia upwelling (e.g., Schott & McCreary, 2001). We also establish that the GW meridional movements have two timescales: a short subseasonal timescale, as pointed out by Beal and Donohue (2013), and a longer "interannual" signal, as underlined by most other authors (Cao & Hu, 2015; Melzer et al., 2019; Trott et al., 2018; Wang et al., 2019). In observations, the GW displays larger southward than northward GW displacements. The potential explanation for this asymmetry remains an open question for future research.

Our study is also in agreement with previous studies that have highlighted the existence of a large contribution of internal variability in this region (Jochum & Murtugudde, 2005; Sengupta et al., 2001) and more specifically a large internal GW variability (Wirth et al., 2002). Another added value of our study is to quantify more precisely the contribution of internal oceanic processes to the subseasonal GW variance (69% over June to September, and up to 81% in September, in agreement with Wirth et al. (2002), who also point out a very strong internal variability in September). We propose that this internal variability is largely related with the intraseasonal variability in the GW position that results from interactions with mesoscale eddies described by Beal and Donohue (2013). We agree with this study that interactions with neighboring meso-scale eddies appear to play an important role in this subseasonal intrinsic variability of the GW. The exact mechanism for this variability probably need to be better understood, and we emphasize that this is an interesting geophysical fluid dynamics problem and a matter that can be investigated using idealized numerical experiments.

Prior to the studies that highlighted its strong internal variability, Luther and O'Brien (1985) proposed that the wind stress forcing was contributing to the GW interannual variability. Our study suggests that there is indeed a forced component to the GW variability, and more specifically to its northward or southward shifts. Of course, this is based on the assumption that the intrinsic variability reduces to zero when performing the ensemble average, which, which is dependent on the size of the ensemble. In fact, this ensemble mean also contains a residual from the intrinsic component (with an amplitude divided by about 7 for our 50-member ensemble). To be more precise, the OCCIPUT ensemble mean fluctuations do not represent only wind-forced but atmospherically forced responses (i.e., including possible responses to heat/freshwater fluxes too), although the wind influence is certainly the main driver of forced GW fluctuations. We believe that our forced component is not heavily influenced by this residual "noise" for two reasons. First, we consider the seasonal-mean forced average in, for example, Figure 9, which means that we increase the number of degrees of freedom by about 4 (considering one independent sample every 20 days), that is, a ∼15-fold reduction in the intrinsic variability residual component. Second, we believe that the verification of a shift in the observed subseasonal GWI probability density for the same years as the shift in the model is an indirect piece of evidence that this mechanism also operates in nature.

Several earlier studies have underlined the possible role of offshore wind stress curl (e.g., Schott & Quadfasel, 1982) and/or Rossby waves radiated from the southwestern coast of India (Beal & Donohue, 2013; Vic et al., 2014) in the GW seasonal cycle. While we agree that the mechanisms are not crystal clear, our study also points to a potential importance of wind stress curl off the coast of Somalia and Rossby Waves in forcing, part of the GW non-seasonal variability. In the absence of a firmly established theory for the formation of the GW itself, it is somewhat difficult to establish a detailed mechanism for its non-seasonal variations. Thus, there is a need for more studies of the GW formation mechanisms, both on seasonal or non-seasonal timescales. We believe that setting up ensemble experiments in an ocean general circulation model forced by idealized wind patterns would probably be a good framework for progress, in the spirit of Vic et al. (2014).

Observed composites of the GW meridional displacements suggest an underestimation by about 30% in our simulations. This underestimation may be related to an underestimation of the forced or intrinsic variability, or both. The estimation of the relative amplitudes of forced and intrinsic variabilities is hence subject to some uncertainty. Wirth et al. (2002) for instance pointed out that the magnitude of the GW internal variability was sensitive to the lateral mixing coefficient. Penduff et al. (2010) also emphasized that the mesoscale variability, which plays a strong role for the intrinsic variability, was underestimated at 1/4° resolution. We analyzed the GW leading mode in two single-member OCCIPUT simulations at 1/12° degree resolution and found that (a) the pattern and amplitude of the GW non-seasonal variability were robust and (b) the difference in amplitude between a simulation forced by either interannual forcing or a repeating seasonal cycle was overall consistent with our estimate of the intrinsic versus forced contributions (not shown). While our results seem to be relatively insensitive to resolution, it may be worth to explore the sensitivity of the GW intrinsic to forced variability ratio to lateral mixing.

The simulations in this study use a forced ocean model. Several previous studies have however underlined a strong air-sea coupling at the scale of the GW, meso-scale, and sub-meso scale SST structures (e.g., Seo, 2017; Seo et al., 2008; Vecchi et al., 2004). Those studies underlined that this air-sea coupling enhances the seasonal water vapor uptake by the atmosphere and has the potential to influence the oceanic evolution at the GW and finer scales. Using a coupled ocean-atmosphere model such as that in Seo (2017) should allow to investigate the mutual influence between air-sea coupling and the GW internal variability.

The main take-home message from our study is that there is a large intrinsic variability component to the GW non-seasonal variability, which is even larger than the forced component for the seasonal mean GW position change based on our quantifications. This means a signal-to-noise ratio of less than one, which may explain why none of the previous studies found a clear link between the GW interannual variability and climate or wind signals (Beal & Donohue, 2013; Cao & Hu, 2015; Melzer et al., 2019; Trott et al., 2018; Wang et al., 2019). We can also examine the dipolar trend in sea surface temperature and height over past three decades discussed by Santos et al. (2015), attributed to a ∼1.5° southward migration of the GW over the last three decades. If the non-seasonal GW signals are purely of intrinsic origin, obtaining such trend by chance would be highly unlikely. The existence of such a trend is hence probably consistent with our results, suggesting that forced GW signals coexist with a larger intrinsic variability component.

Data Availability Statement

The authors confirm that all observational data sets are openly available and their references and download links are provided in Table 1. All data sets and software are cited in the paper and listed in the Reference section. The final processed model output files used for analysis are available at https://doi.org/10.5281/zenodo.10017463, Kwatra (2023). All plots were made using the IDL language (available from https://www.nv5geospatialsoftware.com/Products/IDL), using the SAXO package available at https://forge.ipsl.jussieu.fr/saxo/download/idldoc_html_output/.

Acknowledgments
SK is funded by an ARTS grant from the Institut de Recherche pour le Développement (IRD, France). This research benefitted from funding by the CNES (Centre National d'Etudes Spatiales) "SARAL Altika" project. We acknowledge OCCIPUT (OceaniC Chaos - ImPacts strUcture predicTability project). The OCCIPUT ensemble simulation was achieved using the PRACE Research Infrastructure resource CURIE based in France at TGCC. This work is a contribution to the OCCIPUT and IMHOTEP projects. OCCIPUT has been funded by ANR through contract ANR-13-BS06- 0007-01. IMHOTEP is being funded by CNES through the Ocean Surface Topography Science Team (OSTST). IS acknowledges the funding from CSIR, New Delhi and CSIR-NIO. We thank the Director of CSIR-NIO, the Vice-Chancellor of DUK, and the Vice-Chancelor of Goa University for their support. This is NIO contribution 7190.

References

Anderson, D. L. T. (1981). The Somali current. *Ocean Modelling*, *34*, 6–9.
Beal, L., & Donohue, K. (2013). The Great Whirl: Observations of its seasonal development and interannual variability. *Journal of Geophysical Research: Oceans*, *118*, 1–13. https://doi.org/10.1029/2012JC008198
Berrisford, P., Kållberg, P., Kobayashi, S., Dee, D., Uppala, S., Simmons, A. J., et al. (2011). Atmospheric conservation properties in ERA-Interim. [Dataset]. Quarterly Journal of the Royal Meteorological Society, *137*(659), 1381–1399. https://doi.org/10.1002/qj.864
Bessières, L., Leroux, S., Brankart, J.-M., Molines, J.-M., Moine, M.-P., Bouttier, P.-A., et al. (2017). Development of a probabilistic ocean modelling system based on NEMO 3.5: Application at eddying resolution. *Geoscientific Model Development*, *10*(3), 1091–1106. https://doi.org/10.5194/gmd-10-1091-2017
Bruce, J. G. (1979). Eddies off the Somali coast during the southwest monsoon. *Journal of Geophysical Research*, *84*(C12), 7742–7748. https://doi.org/10.1029/JC084iC12p07742
Cao, Z., & Hu, R. (2015). Research on the interannual variability of the great whirl and the related mechanisms. *Journal of Ocean University of China*, *14*(1), 17–26. https://doi.org/10.1007/s11802-015-2392-8
Cox, M. D. (1979). A numerical study of Somali current eddies. *Journal of Physical Oceanography*, *9*(2), 311–326. https://doi.org/10.1175/1520-0485(1979)009<0311:ANSOSC>2.0.CO;2
Dai, L., Han, B., Tang, S., Chen, C., & Du, Y. (2021). Influences of the Great Whirl on surface chlorophyll a concentration off the Somali Coast in 2017. *Acta Oceanologica Sinica*, *40*(11), 79–86. https://doi.org/10.1007/s13131-021-1740-3
Du, Y., Xie, S. P., Huang, G., & Hu, K. (2009). Role of air–sea interaction in the long persistence of El Niño–induced north Indian Ocean warming. *Journal of Climate*, *22*(8), 2023–2038. https://doi.org/10.1175/2008JCLI2590.1
Dussin, R., Barnier, B., & Brodeau, L. (2016). *The making of Drakkar forcing set DFS5, DRAKKAR/MyOcean Report 01-04-16*. Technical Report. LGGE.
Feldstein, S. B. (2000). The timescale, power spectra, and climate noise properties of teleconnection patterns. *Journal of Climate*, *13*(24), 4430–4440. https://doi.org/10.1175/1520-0442(2000)013<4430:TTPSAC>2.0.CO;2
Findlay, A. G. (1866). *A directory for the navigation of the Indian Ocean, with descriptions of its coasts, islands, etc., from Cape of Good Hope to the Strait of Sunda and Western Australia, including also the Red Sea and the Persian Gulf; the winds, monsoons, and currents, and the passages from Europe to its various ports* (3rd ed.). R.H. Laurie.
Fischer, J., Schott, F., & Stramma, L. (1996). Currents and transports of the Great Whirl-Socotra Gyre system during the summer monsoon, August 1993. *Journal of Geophysical Research*, *101*(C2), 3573–3587. https://doi.org/10.1029/95JC03617
Gentemann, C. L., Meissner, T., & Wentz, F. J. (2010). Accuracy of satellite sea surface temperatures at 7 and 11 GHz. *IEEE Transactions on Geoscience and Remote Sensing*, *48*(3), 1009–1018. https://doi.org/10.1109/tgrs.2009.2030322
Goswami, B. N. (2005). South Asian monsoon. In W. K. M. Lau & D. E. Waliser (Eds.), *Intraseasonal variability in the atmosphere—ocean climate system* (pp. 19–55). Springer.
Hitchcock, G. L., Key, E., & Masters, J. (2000). The fate of upwelled waters in the Great Whirl, August 1995. *Deep-Sea Research II*, *47*(7–8), 1605–1621. https://doi.org/10.1016/S0967-0645(99)00156-3
Hood, R. R., Beckley, L. E., & Wiggert, J. D. (2017). Biogeochemical and ecological impacts of boundary currents in the Indian Ocean. *Progress in Oceanography*, *156*, 290–325. https://doi.org/10.1016/j.pocean.2017.04.011
Izumo, T., Montégut, C. B., Luo, J. J., Behera, S. K., Masson, S., & Yamagata, T. (2008). The role of the western Arabian Sea upwelling in Indian monsoon rainfall variability. *Journal of Climate*, *21*(21), 5603–5623. https://doi.org/10.1175/2008JCLI2158.1
Jensen, T. G. (1993). Equatorial variability and resonance in a wind-driven Indian Ocean model. *Journal of Geophysical Research*, *98*(C12), 22533–22552. https://doi.org/10.1029/93JC02565
Jochum, M., & Murtugudde, R. (2005). Internal variability of Indian ocean SST. *Journal of Climate*, *18*(18), 3726–3738. https://doi.org/10.1175/JCLI3488.1
Kawamiya, M. (2001). Mechanism of offshore nutrient supply in the western Arabian Sea. *Journal of Marine Research*, *59*(5), 675–696. https://doi.org/10.1357/002224001762674890

Knox, R. A., & Anderson, D. L. T. (1985). Recent advances in the study of the low-latitude ocean circulation. *Progress in Oceanography*, *14*, 259–317. https://doi.org/10.1016/0079-6611(85)90014-X

Kwatra, S. (2023). Intrinsic versus wind-forced Great Whirl non-seasonal variability [Dataset]. Zenodo. https://doi.org/10.5281/zenodo.10017463

Leroux, S., Penduff, T., Bessières, L., Molines, J., Brankart, J., Sérazin, G., et al. (2018). Intrinsic and atmospherically forced variability of the AMOC: Insights from a large-ensemble ocean hindcast. *Journal of Climate*, *31*(3), 1183–1203. https://doi.org/10.1175/JCLI-D-17-0168.1

Lorenz, E. N. (1963). Deterministic nonperiodic flow. *Journal of the Atmospheric Sciences*, *20*(2), 130–141. https://doi.org/10.1175/1520-0469(1963)020<0130:DNF>2.0.CO;2

Luther, M. E., & O'Brien, J. J. (1985). A model of the seasonal circulation in the Arabian Sea forced by observed winds. *Progress in Oceanography*, *14*, 353–385. https://doi.org/10.1016/0079-6611(85)90017-5

Madec, G. (2012). *NEMO ocean engine, Note du pôle de modélisation 27*. Institut Pierre Simon Laplace (IPSL).

McCreary, J., & Kundu, P. (1988). A numerical investigation of the Somali Current during the Southwest Monsoon. *Journal of Marine Research*, *46*(1), 25–58. https://doi.org/10.1357/002224088785113711

McCreary, J. P., Han, W., Shankar, D., & Shetye, S. R. (1996). Dynamics of the East India Coastal Current: 2. Numerical solutions. *Journal of Geophysical Research*, *101*, 13993–14010. https://doi.org/10.1029/96JC00560

Melzer, B. A., Jensen, T. G., & Rydbeck, A. V. (2019). Evolution of the Great Whirl using an altimetry-based eddy tracking algorithm. *Geophysical Research Letters*, *46*(8), 4378–4385. https://doi.org/10.1029/2018GL081781

Orúe, B., Pennino, M. G., Lopez, J., Moreno, G., Santiago, J., Ramos, L., & Murua, H. (2020). Seasonal distribution of tuna and non-tuna species associated with drifting fish aggregating devices (DFADs) in the Western Indian Ocean using fishery-independent data. *Frontiers in Marine Science*, *7*, 441. https://doi.org/10.3389/fmars.2020.00441

Palmer, T. N. (1999). A nonlinear dynamical perspective on climate prediction. *Journal of Climate*, *12*(2), 575–591. https://doi.org/10.1175/15200442(1999)012<0575:ANDPOC>2.0.CO;2

Penduff, T., Barnier, B., Terray, L., Bessières, L., Sérazin, G., Gregorio, S., et al. (2014). Ensembles of eddying ocean simulations for climate. *CLIVAR Exchanges*, *65*, 26–29.

Penduff, T., Juza, M., Brodeau, L., Smith, G. C., Barnier, B., Molines, J. M., et al. (2010). Impact of global ocean model resolution on sea-level variability with emphasis on interannual time scales. *Ocean Science*, *6*(1), 269–284. https://doi.org/10.5194/os-6-269-2010

Praveen Kumar, B., Vialard, J., Lengaigne, M., Murty, V. S. N., McPhaden, M. J., Cronin, M. F., et al. (2013). TropFlux wind stresses over the tropical oceans: Evaluation and comparison with other products [Dataset]. Climate Dynamics, *40*(7–8), 2049–2071. https://doi.org/10.1007/s00382-012-1455-4

Resplandy, L., Lévy, M., Madec, G., Pous, S., Aumont, O., & Kumar, D. (2011). Contribution of mesoscale processes to nutrient budgets in the Arabian Sea. *Journal of Geophysical Research*, *116*(C11), C11007. https://doi.org/10.1029/2011JC007006

Reynolds, R. W., Smith, T. M., Liu, C., Chelton, D. B., Casey, K. S., & Schlax, M. G. (2007). Daily high-resolution-blended analyses for sea surface temperature [Dataset]. Journal of Climate, *20*(22), 5473–5496. https://doi.org/10.1175/2007JCLI1824.1

Santos, F., Gomez-Gesteira, M., deCastro, M., & Dıas, J. M. (2015). A dipole-like SST trend in the Somalia region during the monsoon season. *Journal of Geophysical Research: Oceans*, *120*(2), 597–607. https://doi.org/10.1002/2014JC010319

Sathyendranath, S., Grant, M., Brewin, R. J. W., Brockmann, C., Brotas, V., Chuprin, A., et al. (2018). ESA ocean colour climate change initiative (Ocean_Colour_cci): Version 3.1 data [Dataset]. Centre for Environmental Data Analysis. https://doi.org/10.5285/9c334fbe6d424a708cf3c4cf0c6a53f5

Schott, F., & McCreary, J. (2001). The monsoon circulation of the Indian Ocean. *Progress in Oceanography*, *51*(1), 1–123. https://doi.org/10.1016/S0079-6611(01)00083-0

Schott, F., & Quadfasel, D. R. (1982). Variability of the Somali Current system during the onset of the southwest monsoon, 1979. *Journal of Physical Oceanography*, *12*(12), 1343–1357. https://doi.org/10.1175/1520-0485(1982)012<1343:VOTSCS>2.0.CO;2

SeaPAC (2013). *QuikSCAT level 2B ocean wind vectors in 12.5km slice composites version 3*. PO.DAAC. https://doi.org/10.5067/QSX12-L2B01

Sengupta, D., Senan, R., & Goswami, B. N. (2001). Origin of intraseasonal variability of circulation in the tropical central Indian Ocean. *Geophysical Research Letters*, *28*(7), 1267–1270. https://doi.org/10.1029/2000GL012251

Seo, H. (2017). Distinct influence of air–sea interactions mediated by mesoscale sea surface temperature and surface current in the Arabian Sea. *Journal of Climate*, *30*(20), 8061–8080. https://doi.org/10.1175/JCLI-D-16-0834.1

Seo, H., Murtugudde, R., Jochum, M., & Miller, A. J. (2008). Modeling of mesoscale coupled ocean–atmosphere interaction and its feedback to ocean in the western Arabian Sea. *Ocean Modelling*, *25*(3–4), 120–131. https://doi.org/10.1016/j.ocemod.2008.07.003

Sérazin, G., Jaymond, A., Leroux, S., Penduff, T., Bessières, L., Llovel, W., et al. (2017). A global probabilistic study of the ocean heat content low-frequency variability: Atmospheric forcing versus oceanic chaos. *Geophysical Research Letters*, *44*(11), 5580–5589. https://doi.org/10.1002/2017GL073026

Shankar, D., & Shetye, S. R. (1997). On the dynamics of the Lakshadweep high and low in the southeastern Arabian Sea. *Journal of Geophysical Research*, *102*(C6), 12551–12562. https://doi.org/10.1029/97JC00465

Suresh, I., Vialard, J., Izumo, T., Lengaigne, M., Han, W., McCreary, J., & Muraleedharan, P. M. (2016). Dominant role of winds near Sri Lanka in driving seasonal sea level variations along the west coast of India. *Geophysical Research Letters*, *43*(13), 7028–7035. https://doi.org/10.1002/2016GL069976

Suresh, I., Vialard, J., Lengaigne, M., Han, W., McCreary, J., Durand, F., & Muraleedharan, P. M. (2013). Origins of wind-driven intraseasonal sea level variations in the North Indian Ocean coastal waveguide. *Geophysical Research Letters*, *40*(21), 5740–5744. https://doi.org/10.1002/2013GL058312

Suresh, I., Vialard, J., Lengaigne, M., Izumo, T., Parvathi, V., & Muraleedharan, P. M. (2018). Sea level interannual variability along the west coast of India. *Geophysical Research Letters*, *45*(22), 12440–12448. https://doi.org/10.1029/2018GL080972

Swallow, J. C., & Bruce, J. G. (1966). Current measurements off the Somali coast during the southwest monsoon of 1964. *Deep-Sea Research and Oceanographic Abstracts*, *13*(5), 861–888. https://doi.org/10.1016/0011-7471(76)90908-6

Swallow, J. C., & Fieux, M. (1982). Historical evidence for two gyres in the Somali Current. *Journal of Marine Research*, *40*, 747–755.

Taburet, G., Sanchez-Roman, A., Ballarotta, M., Pujol, M.-I., Legeais, J.-F., Fournier, F., et al. (2019). DUACS DT2018: 25 years of reprocessed sea level altimetry products [Dataset]. Ocean Science, *15*(5), 1207–1224. https://doi.org/10.5194/os-15-1207-2019

Trott, C. B., Subrahmanyam, B., Chaigneau, A., & Delcroix, T. (2018). Eddy tracking in the northwestern Indian Ocean during southwest monsoon regimes. *Geophysical Research Letters*, *45*(13), 6594–6603. https://doi.org/10.1029/2018GL078381

Trott, C. B., Subrahmanyam, B., & Murty, V. S. N. (2017). Variability of the Somali Current and eddies during the southwest monsoon regimes. *Dynamics of Atmospheres and Oceans*, *79*, 43–55. https://doi.org/10.1016/j.dynatmoce.2017.07.002

Vecchi, G., Xie, S., & Fischer, A. (2004). Ocean-atmosphere covariability in the western Arabian Sea. *Journal of Climate*, *17*(6), 1213–1224. https://doi.org/10.1175/1520-0442(2004)017<1213:OCITWA>2.0.CO;2

Vic, C., Capet, X., Roullet, G., & Carton, X. (2017). Western boundary upwelling dynamics off Oman. *Ocean Dynamics*, *67*(5), 585–595. https://doi.org/10.1007/s10236-017-1044-5

Vic, C., Roullet, G., Carton, X., & Capet, X. (2014). Mesoscale dynamics in the Arabian Sea and a focus on the Great Whirl life cycle: A numerical investigation using ROMS. *Journal of Geophysical Research: Oceans*, *119*(9), 6422–6443. https://doi.org/10.1002/2014JC009857

Vinayachandran, P. N. M., Masumoto, Y., Roberts, M. J., Huggett, J. A., Halo, I., Chatterjee, A., et. al. (2021). Reviews and syntheses: Physical and biogeochemical processes associated with upwelling in the Indian Ocean. *Biogeosciences*, *18*(22), 5967–6029. https://doi.org/10.5194/bg-18-5967-2021

Wang, S., Zhu, W., Ma, J., Ji, J., Yang, J., & Dong, C. (2019). Variability of the great whirl and its impacts on atmospheric processes. *Remote Sensing*, *11*(3), 322. https://doi.org/10.3390/rs11030322

Wirth, A., Willebrand, J., & Schott, F. (2002). Variability of the Great Whirl from observations and models. *Deep Sea Research II*, *49*(7), 1279–1295. https://doi.org/10.1016/S0967-0645(01)00165-5

Xie, S. P., Hu, K., Hafner, J., Tokinaga, H., Du, Y., Huang, G., & Sampe, T. (2009). Indian Ocean capacitor effect on Indo–western Pacific climate during the summer following El Niño. *Journal of Climate*, *22*(3), 730–747. https://doi.org/10.1175/2008JCLI2544.1

Young, D. K., & Kindle, J. C. (1994). Physical processes affecting availability of dissolved silicate for diatom production in the Arabian Sea. *Journal of Geophysical Research*, *99*(C11), 22619–22632. https://doi.org/10.1029/94JC01449

Zhan, P., Guo, D., & Hoteit, I. (2020). Eddy-induced transport and kinetic energy budget in the Arabian Sea. *Geophysical Research Letters*, *47*(23), e2020GL090490. https://doi.org/10.1029/2020GL090490